Molecular Therapy
Original Article

Engineering a targeted and safe bone anabolic gene therapy to treat osteoporosis in alveolar bone loss

Chujiao Lin,[1] Yeon-Suk Yang,[1] Hong Ma,[2,3,4] Zhihao Chen,[1] Dong Chen,[5,6] Aijaz Ahmad John,[1] Jun Xie,[2,3,4] Guangping Gao,[2,3,4,7] and Jae-Hyuck Shim[1,3,7]

[1]Department of Medicine/Division of Rheumatology, UMass Chan Medical School, Worcester, MA 01655, USA; [2]Department of Microbiology and Physiological Systems, UMass Chan Medical School, Worcester, MA 01655, USA; [3]Horae Gene Therapy Center, Umass Chan Medical School, Worcester, MA 01655, USA; [4]Viral Vector Core, UMass Chan Medical School, Worcester, MA 01655, USA; [5]State Key Laboratory of Oral & Maxillofacial Reconstruction and Regeneration, Key Laboratory of Oral Biomedicine Ministry of Education, Hubei Key Laboratory of Stomatology, School & Hospital of Stomatology, Wuhan University, Wuhan 430079, China; [6]Department of Implantology, School & Hospital of Stomatology, Wuhan University, Wuhan 430079, China; [7]Li Weibo Institute for Rare Diseases Research, UMass Chan Medical School, Worcester, MA 01655, USA

Alveolar bone loss in elderly populations is highly prevalent and increases the risk of tooth loss, gum disease susceptibility, and facial deformity. Unfortunately, there are very limited treatment options available. Here, we developed a bone-targeted gene therapy that reverses alveolar bone loss in patients with osteoporosis by targeting the adaptor protein Schnurri-3 (SHN3). SHN3 is a promising therapeutic target for alveolar bone regeneration, because SHN3 expression is elevated in the mandible tissues of humans and mice with osteoporosis while deletion of SHN3 in mice greatly increases alveolar bone and tooth dentin mass. We used a bone-targeted recombinant adeno-associated virus (rAAV) carrying an artificial microRNA (miRNA) that silences SHN3 expression to restore alveolar bone loss in mouse models of both postmenopausal and senile osteoporosis by enhancing WNT signaling and osteoblast function. In addition, rAAV-mediated silencing of SHN3 enhanced bone formation and collagen production of human skeletal organoids in xenograft mice. Finally, rAAV expression in the mandible was tightly controlled via liver- and heart-specific miRNA-mediated repression or via a vibration-inducible mechanism. Collectively, our results demonstrate that AAV-based bone anabolic gene therapy is a promising strategy to treat alveolar bone loss in osteoporosis.

INTRODUCTION

Alveolar bone is the portion of the mandibular and maxillary bones that not only supports the tooth sockets and muscles of mastication but also protects nerves, vessels, and glands.[1,2] It undergoes rapid bone remodeling during tooth eruption due to the forces of mastication and positional adaptation of the teeth.[3,4] Normal alveolar bone remodeling is controlled by bone-forming osteoblasts and bone-resorbing osteoclasts, but disruption of that balance leads to alveolar bone atrophy.[5] Osteoporosis frequently develops atrophic alveolar bone[6] and hampers proper chewing and speaking, heightens vulnerability to gum disease, and disrupts tooth alignment associated with facial deformity.[7] Additionally, reduced alveolar bone density makes dental implant procedures challenging, as they require sufficient bone mass to achieve dental implantation.[8,9] Therefore, preserving alveolar bone health is crucial for maintaining optimal oral health, function, and aesthetics.

Restoration of alveolar bone loss in osteoporosis poses a significant challenge in dental practice. Current treatments include anti-inflammatory agents[10] and the transplantation of natural or synthetic bone grafts[11,12] and resorbable or non-resorbable collagen membranes along with supplementary bioactive products.[13,14] Additionally, osteoporosis drugs, such as bisphosphonates,[15] anti-RANKL antibody,[16] parathyroid hormone analogs,[17] and estrogen replacement,[18] are used for treatment. However, these treatments show limited success in the clinic due to a lack of long-term preservation, rehabilitation, and functional needs of alveolar bone.[19] Moreover, while oral administration of bisphosphonates does not show significant improvement in preventing alveolar bone loss, bisphosphonates can cause oral bony lesions such as bisphosphonate-related osteonecrosis of the jaw.[20,21] Surgical transplantation often fails and frequently leads to complications. For example, vertical bone augmentation is hindered by brittleness and inadequate toughness in newly formed bones, resulting in frequent fractures during the implantation process.[22] The use of

Received 24 February 2024; accepted 24 June 2024;
https://doi.org/10.1016/j.ymthe.2024.06.036.

Correspondence: Guangping Gao, Horae Gene Therapy Center, Li Weibo Institute for Rare Diseases Research, UMass Chan Medical School, 368 Plantation Street, AS6-2049, Worcester, MA 01605, USA.
E-mail: guangping.gao@umassmed.edu
Correspondence: Jae-Hyuck Shim, Department of Medicine/Division of Rheumatology, Horae Gene Therapy Center, Li Weibo Institute for Rare Diseases Research, UMass Chan Medical School, 364, Plantation Street, LRB-217, Worcester, MA 01605, USA.
E-mail: jaehyuck.shim@umassmed.edu

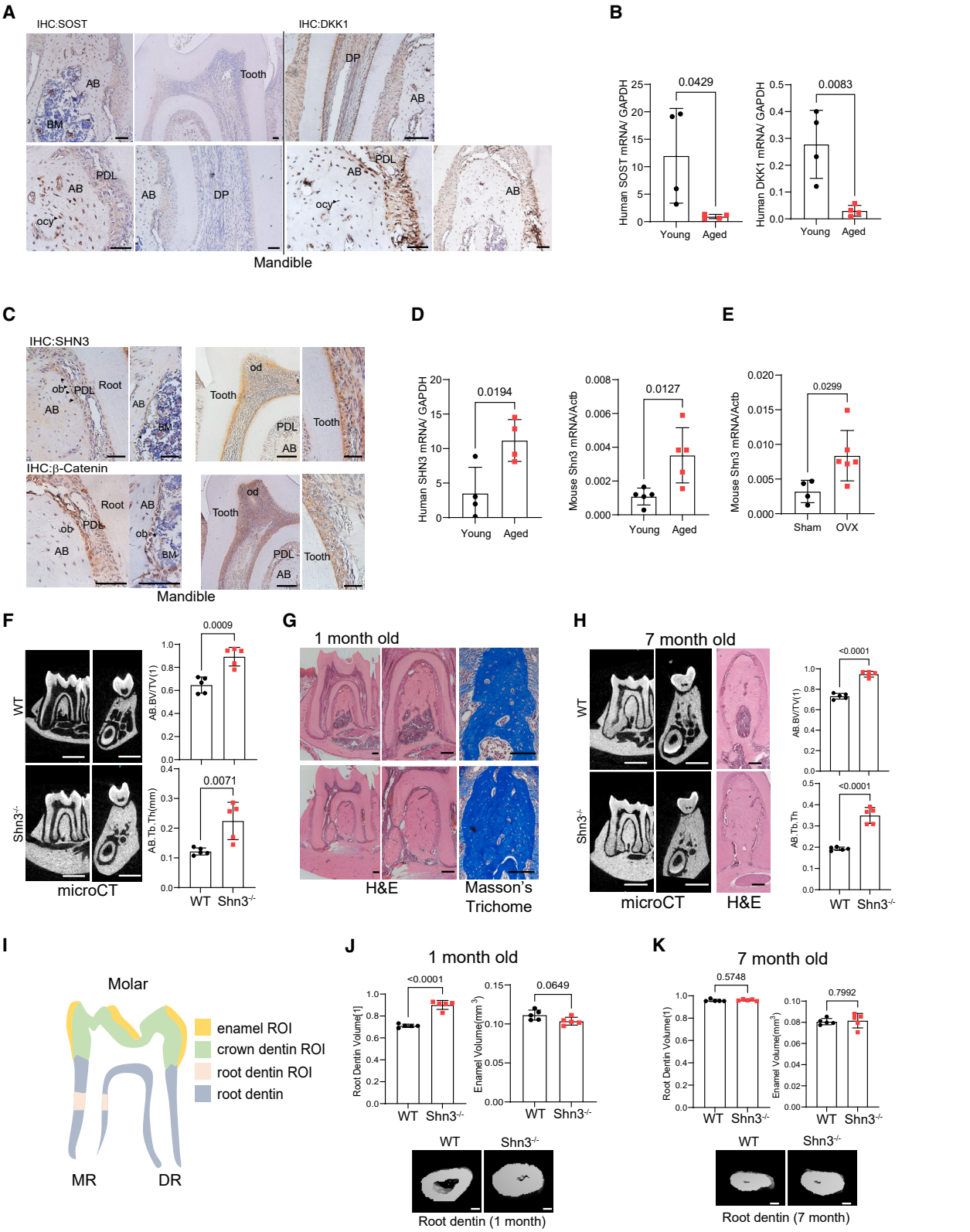

(legend on next page)

slow-resorbing bone biomaterials also can compromise the quantity and quality of newly formed bone in augmentation sites.[23] Hence, the development of new therapeutics to restore alveolar bone loss while limiting worrisome side effects remains an unmet need.

Recombinant adeno-associated viruses (rAAV) have demonstrated long-term durability of gene expression, lack of post-immunogenicity, and good safety profiles in clinical studies.[24] Although rAAVs have targeted various organs, such as brain, eye, heart, liver, and skeletal muscle, rAAV-mediated gene therapy for craniofacial diseases has not been evaluated.[25] Our prior work demonstrated rAAV9 as a highly effective serotype for transducing osteoblast-lineage cells in the long bones and vertebrae of mice.[26] Here, we tested the ability of rAAV9 to promote alveolar bone regeneration by targeting Schnurri-3 (SHN3), an intracellular adaptor protein involved in WNT signaling that inhibits bone formation.[27,28] We demonstrate that rAAV-mediated gene therapy targeting SHN3 is an alternative approach to traditional osteoporosis drugs to reverse alveolar bone loss in osteoporotic patients. A bone-targeted AAV effectively delivered a SHN3 silencer to osteoblast-lineage cells that reside in alveolar bone, enhanced WNT signaling and osteoblast function, and promoted alveolar bone formation in osteoporotic mice. Moreover, rAAV expression in non-skeletal organs, heart, and liver was repressed via organ-specific miRNA-mediated degradation while the expression was tightly controlled in a vibration-inducible manner. Thus, the bone-trophic AAV targeting SHN3 is a promising bone anabolic agent that restores alveolar bone loss in osteoporosis while limiting potential side effects.

RESULTS

SHN3 deletion increases alveolar bone and tooth dentin mass

The WNT pathway is a key regulator of bone formation by enhancing osteoblast development, and WNT antagonists, such as sclerostin (SOST),[29] dickkopf-1 (DKK-1),[30] and schnurri-3 (SHN3),[31] are promising targets to promote bone formation in osteoporosis. While SOST and DKK-1 proteins are all present in the alveolar bone in young mice (Figure 1A), mRNA expression of *SOST* and *DKK-1* was substantially decreased in older human mandibles relative to young mandibles (Figure 1B). Accordingly, treatment of aged osteoporotic rats with anti-SOST antibody or anti-DKK-1 antibodies showed minimal effects on alveolar bone regeneration.[32–34] SHN3 expression was also detected in the alveolar bone of young mice (Figure 1C), but unlike SOST and DKK1, its expression was further upregulated in human and mouse aged mandibles (Figure 1D). Similarly, postmenopausal osteoporosis in female mice also increased *Shn3* expression in mandibles (Figure 1E). Thus, SHN3 is likely to be a more attractive target than SOST and DKK1 for alveolar bone regeneration in osteoporotic settings.

SHN3 controls β-Catenin stability downstream of WNT signaling and deleting SHN3 enhances WNT signaling, osteoblast development, and bone formation.[27] Thus, we hypothesized that SHN3 may play a role in alveolar bone development by regulating WNT signaling. To explore potential regulatory interactions between SHN3 and WNT signaling within the alveolar bone, an immunohistochemistry (IHC) analysis was performed, demonstrating co-localization of SHN3 and β-Catenin in multiple cell populations within alveolar bone, including periodontal ligament cells (PDLs), odontoblasts (ODs), osteoblasts (OBs), and osteocytes (OCYs, Figure 1C). MicroCT analysis of alveolar bone demonstrated greater bone volume per tissue volume (BV/TV) and trabecular bone thickness (Tb.Th) in 1-month-old $Shn3^{-/-}$ mice than littermate controls (Figure 1F). This is consistent with a histologic analysis showing an increase in trabecular bone mass in the bone marrow of $Shn3^{-/-}$ mandibles (Figure 1G). Seven-month-old $Shn3^{-/-}$ mice also showed an increase in alveolar bone mass, but this increase was slightly compromised as trabecular bone mass became saturated (Figure 1H). These results suggest that SHN3 acts as a key regulator of alveolar bone mass during skeletal development and homeostasis.

SHN3 expression in dentin-producing odontoblasts within mandibles prompted us to test its potential role in dental development. MicroCT analysis of the mandibular first molar demonstrated a significant increase in root dentin volume in 1-month-old $Shn3^{-/-}$ mice relative to littermate controls, while enamel volume, produced by dental ameloblasts, was comparable between $Shn3^{-/-}$ and littermate control mice (Figures 1I and 1J). Notably, the increase in root dentin volume of $Shn3^{-/-}$ mice was halted as dentin production was saturated at the age of 7 months (Figure 1K). These results suggest that SHN3 in odontoblasts functions as a suppressor of dentin production at early

Figure 1. SHN3 deletion increases alveolar bone and tooth root dentin mass

(A and C) Immunohistochemistry showing expression of SOST and DKK1 (A) and SHN3 and β-Catenin (C) in the mandible of 2-month-old mice. AB: alveolar bone, PDL: periodontal ligament, BM: bone marrow, DP: dental pulp, ob, osteoblasts, od: odontoblasts, ocy: osteocytes.

(B and D) Human *SOST*, *DKK1*, and *SHN3* mRNA expression in the mandible of young vs. aged patients (n = 4/group). (E) Mouse *Shn3* mRNA expression in the mandible of 2-month-old vs. 24-month-old mice (n = 5/group, left) and 6-month-old mice with sham control vs. ovariectomy (OVX) surgery (n = 4–6/group, right). (F–H) MicroCT and histologic analyses showing alveolar bone mass in the first molar of 1- and 7-month-old $Shn3^{-/-}$ and $Shn3^{+/+}$ (WT) mandibles. MicroCT images showing sagittal and cross sections of the first molar (F, left and middle; H, left). H&E (G, left and middle; H, middle) and Masson's trichrome staining of sagittal sectioned molar (G, right). MicroCT quantification of alveolar bone mass in the first molar (n = 5/group, F, left). AB.BV/TV: alveolar bone volume per tissue volume, AB.Th: alveolar bone thickness (F, right). (J and K) MicroCT analysis showing root dentin and enamel volume of the first molar of 1- and 7-month-old $Shn3^{-/-}$ and $Shn3^{+/+}$ mandible. 3D-reconstruction images (J, K-bottom) and relative quantification (n = 5/group) are displayed (J, K-top). The representative image of the methods used to quantitatively measure the parameters listed in (I) The area highlighted in green marks the crown dentin region of interest (ROI), the yellow area marks the enamel ROI, the pink area marks the root dentin ROI, and the gray area marks the root dentin. MR: mesial root, DR: distal root. Scale bars: 50 μm (A and C), 1 mm (F, left and middle; H, left), 100 μm (G and H, middle; J, bottom; K, bottom). A two-tailed unpaired Student's t test for comparing two groups: (B), (D), (E), (F), (H), (J), and (K); error bars, data represent mean ± SD. Representative images of three replicates are displayed (A, C, G, H, J, K).

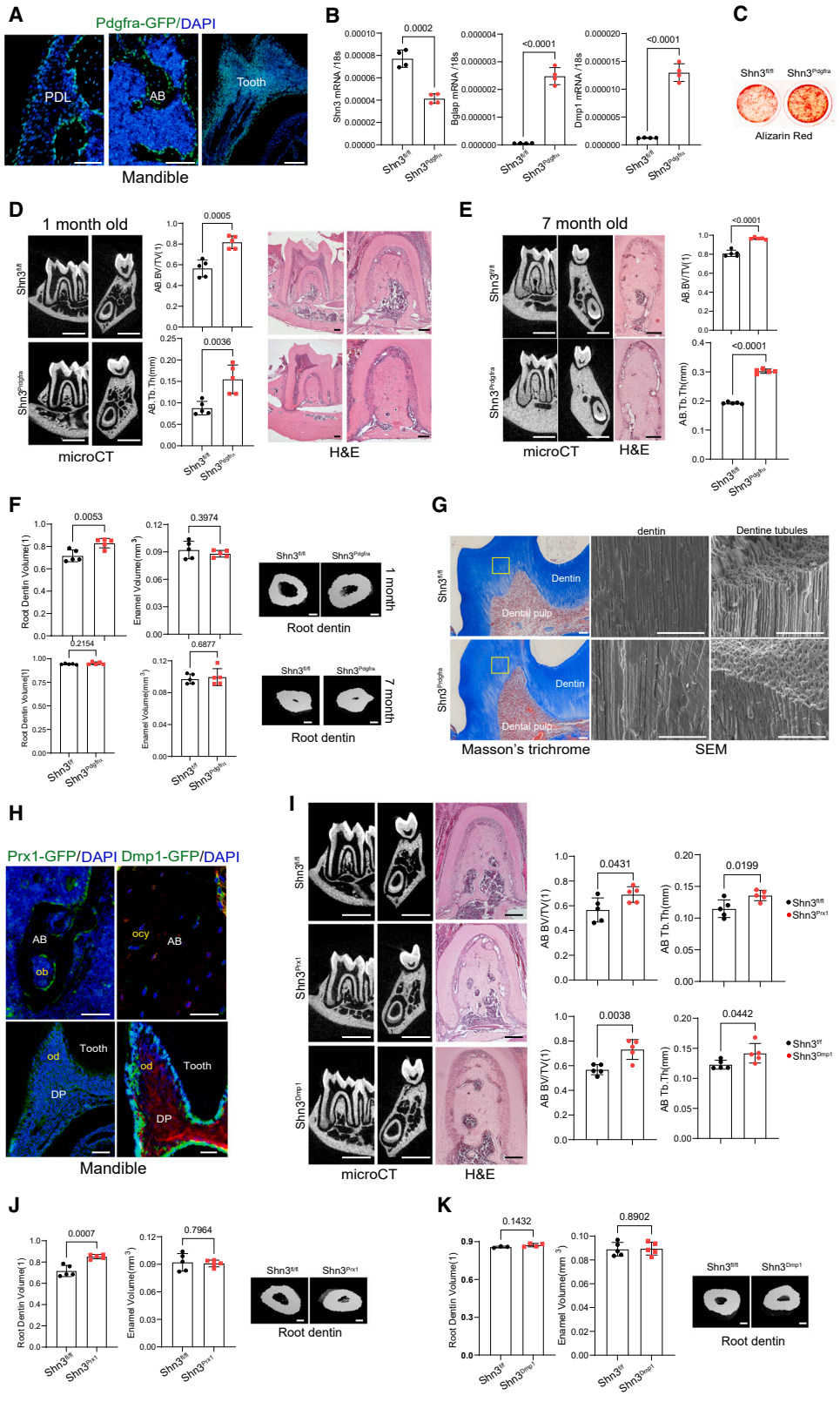

(legend on next page)

developmental stages while its role in ameloblasts is dispensable for enamel production. Thus, SHN3 is crucial for alveolar bone and tooth dentin formation, which makes SHN3 an attractive therapeutic target to promote regeneration of alveolar bone and tooth dentin.

SHN3 deletion in mesenchyme-lineage cells increases alveolar bone and tooth dentin mass

Platelet-derived growth factor receptors (PDGFRs) have been reported to express in a broad range of mesenchyme-lineage cells at multiple anatomical locations in the skeleton.[35,36] Fluorescence microscopy of Pdgfrα-GFP reporter mice demonstrated GFP expression in periodontal ligament cells, osteoblast-lineage cells, and dental-lineage cells within mandibles (Figure 2A). *Shn3* was conditionally deleted in these cells by crossing mice with a *Shn3*-floxed allele ($Shn3^{fl/fl}$) with *Pdgfrα-Cre* mice ($Shn3^{Pdgfr\alpha}$). Reduced expression of *Shn3* was confirmed in alveolar bone-derived mesenchymal stromal cells (ABMSCs) isolated from $Shn3^{Pdgfr\alpha}$ mandibles (Figure 2B). These cells showed an increase in expression of osteogenic marker genes, including osteocalcin (*Bglap*) and dentin matrix acidic phosphoprotein 1 (*Dmp1*, Figure 2B), and extracellular mineralization (alizarin red staining, Figure 2C), indicating enhanced osteogenic activity. As seen in $Shn3^{-/-}$ mice, alveolar bone mass was markedly increased in $Shn3^{Pdgfr\alpha}$ mice relative to littermate controls ($Shn3^{fl/fl}$) at ages 1 and 7 months, as shown by increased BV/TV and Tb.Th. This is consistent with a histologic analysis showing an increase in trabecular bone mass in the bone marrow of $Shn3^{Pdgfr\alpha}$ mandibles (Figures 2D and 2E). Similarly, trabecular bone mass and cortical thickness in the long bones were both markedly increased in these mice (Figure S1A). These results highlight the role of SHN3 in $Pdgfr\alpha^{+}$ cells as a key regulator of alveolar and long bone mass during skeletal development and homeostasis.

Since Pdgfrα-GFP expression was also detected in odontoblasts within mandibles (Figure 2A), we assessed the tooth dentin volume in the first molar of $Shn3^{Pdgfr\alpha}$ mandibles using microCT. Similar to $Shn3^{-/-}$ mandibles, 1-month-old $Shn3^{Pdgfr\alpha}$ mandibles displayed a significant increase in root dentin volume without any alteration in enamel volume and the increased root dentin volume was halted as dentin production was saturated at the age of 7 months (Figure 2F). Notably, Masson's trichrome staining and scanning electron microscopy (SEM) of $Shn3^{Pdgfr\alpha}$ tooth showed normal dentin matrix and tubular structure, showing that *Shn3* deletion in $Pdgfr\alpha^{+}$ cells leads to an increase in a good quality of dentin mass (Figure 2G).

Next, SHN3 expression was deleted at early and late stages of osteoblast differentiation by crossing $Shn3^{fl/fl}$ mice with *Prx1-Cre* mice ($Shn3^{Prx1}$) and *Dmp1-Cre* mice ($Shn3^{Dmp1}$), respectively. *Prx1-Cre* mice and *Dmp1-Cre* mice were also crossed with *Rosa26* $^{mT/mG}$ reporter mice[37] where Cre-recombinase uses GFP expression to visualize Cre-expressing cells within mandibles. Unlike Prx1-GFP proteins primarily expressed in osteoblasts on the alveolar bone surface, Dmp1-GFP expression was detected in osteocytes embedded in the alveolar bone matrix. Prx1- and Dmp1-GFP proteins were both expressed in odontoblasts on the dentin surface (Figure 2H). Deletion of *Shn3* in $Prx1^{+}$ skeletal progenitors and $Dmp1^{+}$ osteocytes resulted in a significant increase in alveolar bone mass (Figure 2I) and femoral bone mass (Figures S1B and S1C). These results show that SHN3 acts in both early and late stages of osteoblast differentiation to produce alveolar bone and long bone. One-month-old $Shn3^{Prx1}$ mandibles displayed an increase in root dentin volume of the first molar without any change in enamel volume (Figure 2J). However, there was little to no increase in root dentin volume in $Shn3^{Dmp1}$ molars (Figures 2J and 2K), showing that SHN3 in skeletal progenitors, but not in osteocytes, drives dentin production during skeletal development. Thus, inhibition of SHN3 in skeletal progenitors promotes formation of long bone, alveolar bone, and tooth dentin.

AAV-mediated silencing of human SHN3 promotes bone formation in xenograft mice

To test whether SHN3-deficiency in human osteoblasts can promote bone formation, human artificial miRNA (*hs-amiR*) was developed by embedding the guide strand of a small silencing RNA that targets

Figure 2. Mesenchyme-specific deletion of SHN3 increases alveolar bone and tooth root dentin mass

(A) Fluorescence microscopy was performed on cryo-sectioned mandibles from 2-month-old *Pdgfrα-GFP* reporter mice to visualize GFP-expressing Pdgfrα-lineage cells in the alveolar bone and tooth.

(B and C) Alveolar bone marrow mesenchymal stromal cells (ABMSCs) were isolated from the mandible of 4-week-old $Shn3^{Pdgfr\alpha}$ and $Shn3^{fl/fl}$ mice and cultured under osteogenic conditions. mRNA expression of *Shn3, Bglap*, and *Dmp1* (B) and mineralization activity (C) were assessed by RT-PCR and alizarin red staining, respectively (n = 4/group). (D and E) MicroCT and histologic analyses showing alveolar bone mass in the first molar of 1- and 7-month-old $Shn3^{Pdgfr\alpha}$ and $Shn3^{fl/fl}$ mandibles. MicroCT images showing sagittal and cross sections of the mandibular first molar (left). H&E staining of sagittal sectioned molar (D, right; E, middle). MicroCT quantification of alveolar bone mass in the mandibular first molar (n = 5/group, D, middle; E, right). (F) MicroCT analysis showing root dentin and enamel volume of the first molar of 1- or 7- month-old $Shn3^{Pdgfr\alpha}$ and $Shn3^{fl/fl}$ mandibles. 3D-reconstruction images and relative quantification (n = 5/group) are displayed. (G) Masson's trichome staining (left) and scanning electron microscopy (SEM, right) were performed in sagittal sectioned tooth dentin of the first molar of 1-month-old $Shn3^{Pdgfr\alpha}$ and $Shn3^{fl/fl}$ mandibles, demonstrating normal microstructure of tooth dentin.

(H) Fluorescence microscopy was performed on cryo-sectioned mandibles from 2-month-old *Prx1-GFP* (left) and *Dmp1-cre;Rosa26*^{mTmG} (right) reporter mice to visualize GFP-expressing Prx1-or Dmp1-lineage cells in the alveolar bone and tooth. (I) MicroCT and histologic analyses showing alveolar bone mass in the first molar of 1-month-old $Shn3^{Dmp1}$, $Shn3^{Prx1}$, and $Shn3^{fl/fl}$ mandibles. MicroCT images (left), H&E staining (middle), and microCT quantification of alveolar bone mass in the molar (right) are displayed (n = 5/group). (J and K) MicroCT analysis showing root dentin and enamel volume of the first molar of 1-month-old $Shn3^{Prx1}$, $Shn3^{Dmp1}$, and $Shn3^{fl/fl}$ mandibles. 3D-reconstruction images and relative quantification (n = 5/group) are displayed. Scale bars: 50 μm (A; G, left; H), 1 mm (D; E, left; I, left), 100 μm (D, right; E, middle; F, right; I-middle, J-right, K-right), 30 μm (G, right). A two-tailed unpaired Student's t test for comparing two groups (B, D, E, F, I, J, K; error bars, data represent the mean ± SD). Representative images of three replicates are displayed (A, C, D, E–K).

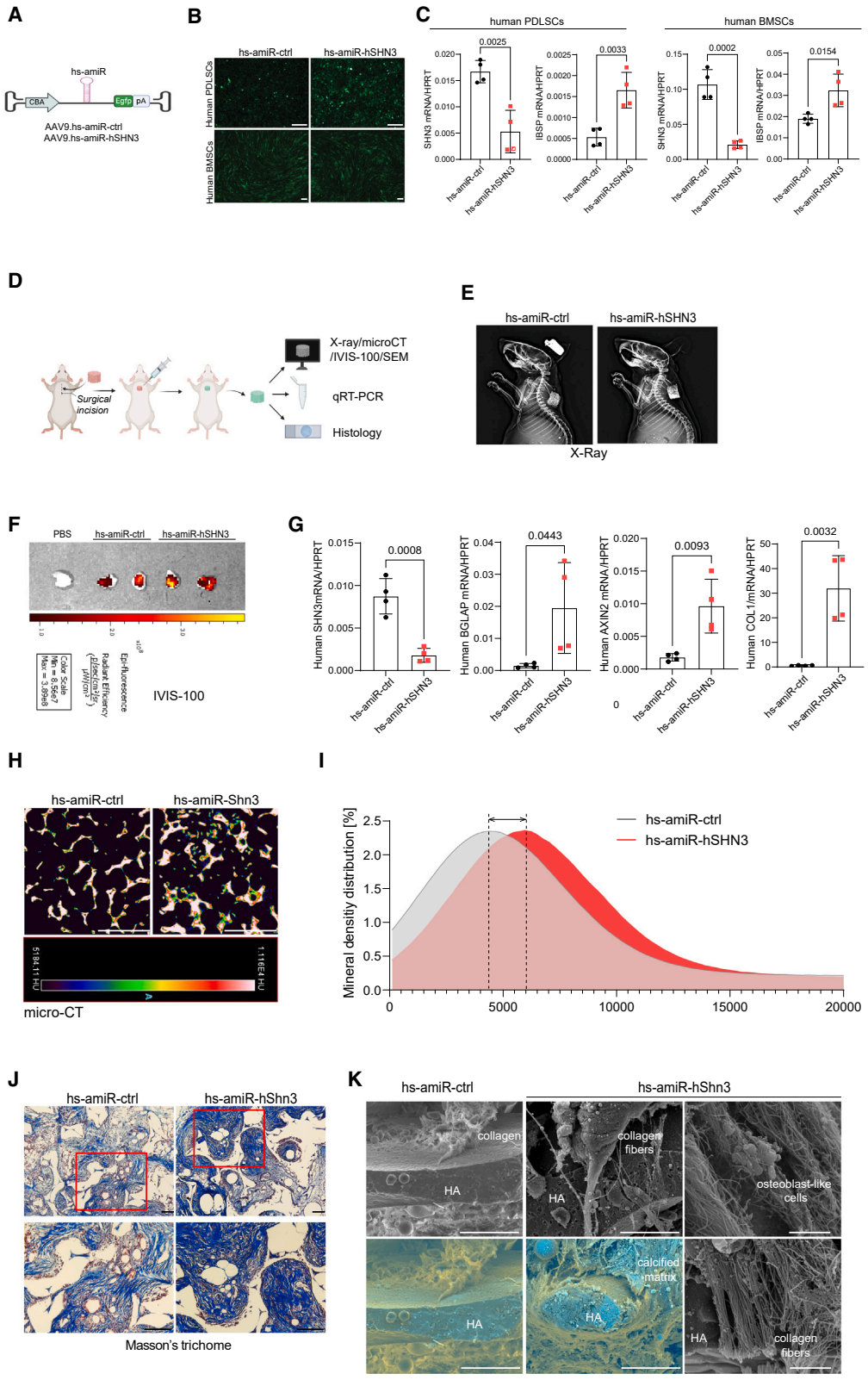

(legend on next page)

human *SHN3* into a human miR-33-derived miRNA scaffold (*hs-amiR-hSHN3*),[38] and then packaged into the AAV9 capsid. In this design, the *hs-amiR* is inserted intronically between the chicken β-actin (*CBA*) promoter and the *Egfp* reporter gene[39] (Figure 3A), which allows for visual tracking of positively transduced cells or tissues. The AAV9's ability to transduce human periodontal ligament stromal cells (PDLSCs) or bone marrow-derived mesenchymal stromal cells (BMSCs) was confirmed by GFP expression using fluorescence microscopy (Figure 3B). rAAV9 carrying *hs-amiR-hSHN3* effectively silenced *SHN3* expression in these cells and increased osteogenic differentiation (Figure 3C). Next, we examined whether AAV-mediated silencing of human *SHN3* promotes bone formation *in vivo* using a xenograft mouse model implanted with a human skeletal organoid (Figure 3D). The human skeletal organoid was generated by culturing human BMSCs in hydroxyapatite (HA)-scaffold under osteogenic conditions and then implanted into interscapular fat pads of immunodeficient mice (Figure 3E). A single dose of rAAV9 carrying *hs-amiR-ctrl* or *hs-amiR-hSHN3* was injected to the implanted site. Four weeks later, AAV's ability to transduce the human skeletal organoid and to knock down *Shn3* expression was confirmed by GFP expression using the IVIS optical imaging system (Figure 3F) and RT-PCR analysis (Figure 3G), respectively. Compared with *hs-amiR-ctrl, hs-amiR-hSHN3* treatment markedly increased osteogenic gene expression, osteocalcin (*BGLAP*) and type 1 collagen (*COL1*), and WNT-induced gene expression, *AXIN2* (Figure 3G). Likewise, this organoid showed a significant increase in mineral density distribution (microCT) and newly formed collagen and mineral (Masson's trichrome staining, Figures 3H–3J). This is consistent with SEM showing increased production of collagen fibers and calcified matrix in the human skeletal organoid at molecular levels (Figure 3K). Thus, AAV-mediated silencing of SHN3 is effective in transducing human osteoblast-lineage cells, enhancing osteogenic differentiation and WNT signaling and promoting bone formation in human skeletal organoids, suggesting the clinical potential to human skeletal diseases with low bone mass.

AAV-mediated silencing of *Shn3* reverses alveolar bone loss in osteoporosis

Since rAAV9 has been reported as a highly effective serotype that transduces osteoblast-lineage cells in the long bone and vertebrae in mice,[40] rAAV9's ability to transduce alveolar bone was examined using GFP expression after intravenous (i.v.) injection or periodontal ligament (PL) injection to the mandibular first molar (Figure S2A, top and S2B). Individual organ imaging of i.v.-injected mice showed robust GFP expression in liver and muscle and a modest expression in the mandible. By contrast, PL-injected mice showed a modest expression in the liver and mandible with little to no expression in muscle, brain, heart, lung, spleen, and kidney (Figure 4A). This is consistent with RT-PCR analysis and fluorescence microscopy on cryosectioned tissues showing a significant decrease in GFP expression in the liver, heart, and muscle when treated via PL injection relative to i.v. injection (Figures 4B and S2C). However, GFP expression in the PL-injected mandibles was increased 3-fold (Figure 4C) when rAAV9 was transduced into periodontal ligament cells, odontoblasts, and osteoblast-lineage cells (Figure S2D). Thus, PL injection of rAAV9 is an effective gene delivery strategy to transduce alveolar bone while limiting AAV's expression in other tissues.

To further improve the bone-specific tropism of the rAAV9 capsid, a bone-homing peptide motif $(AspSerSer)_6$ was grafted onto an AAV9-VP2 capsid protein (dss.rAAV9).[26,41] Eight-week-old Pdgfrα-GFP reporter mice were treated with mCherry-expressing dss.rAAV9 (dss.rAAV9.mCherry) via PL injection into the mandibular first molar and mCherry expression in Pdgfrα-GFP$^+$ cells was assessed by fluorescence microscopy. Fluorescence microscopy showed mCherry expression in a subset of Pdgfrα$^+$ cells in alveolar bone, including PL cells, osteoblast-lineage cells, and odontoblasts (Figure 4D). Thus, PL injection of dss.rAAV9 effectively transduces Pdgfrα$^+$ alveolar bone-residing cells.

Postmenopausal osteoporosis results in alveolar bone loss and deterioration of bone structure, increasing the risk of tooth loss, gum disease susceptibility, and facial deformity.[42,43] This process can be modeled in mice; ovariectomy (OVX) surgery in female mice leads to estrogen deficiency-induced bone loss, recapitulating postmenopausal osteoporosis.[44] To test whether AAV-mediated silencing of *Shn3* can reverse alveolar bone loss in postmenopausal osteoporosis, we generated an AAV-compatible artificial miRNA that silences mouse *Shn3* expression by embedding *Shn3*-targeting sequences into a mouse miR-33-derived miRNA scaffold (*amiR-SHN3*,

Figure 3. AAV-mediated silencing of human SHN3 increases bone and collagen formation

(A) The AAV vector genome containing the CMV enhancer/chicken β-actin promoter (*CBA*), *hs-amiR-ctrl*, *hs-amiR-hSHN3*, an *Egfp* reporter gene (EGFP), *β-globin* polyA sequence (PA), and inverted terminal repeat (ITR) was packaged into the rAAV9 capsid. (B and C) Human periodontal ligament stem cells (hPDLCs) and bone marrow-derived stromal cells (hBMSCs) were treated with rAAV9 carrying *hs-amiR-ctrl* or *hs-amiR-hShn3* (4×10^6 vg/cell) and cultured under osteogenic conditions for 4 days. rAAV9's transduction efficiency was examined by fluorescence microscopy using EGFP expression (B). mRNA expression of *SHN3* and the osteogenic marker *IBSP* were assessed by RT-PCR ($n = 4$/group, C). (D–J) Diagram of the study and treatment methods. Human BMSC-seeded hydroxyapatite (HA)-scaffold was implanted into the interscapular fat pads of immunodeficient SCID mice and 1 week later, PBS or rAAV9 carrying *hs-amiR-ctrl* or *hs-amiR-hSHN3* (2.5×10^{12} vg/kg) was injected into the implantation site (D). Four weeks later, the implanted scaffold was visualized by radiography (E), and EGFP expression in the scaffold was assessed by IVIS-100 optical imaging system (F). mRNA expression of *SHN3, BGLAP, AXIN2*, and *COL1* in the scaffold was assessed by RT-PCR ($n = 4$/group, G). Bone accrual and collagen production of the scaffold were assessed by microCT (H and I), histology (J), and SEM (K). 2D microCT images (H) and relative quantification showing mineral density distribution (I) are displayed. Masson's trichome staining shows a significant increase in collagen production in the *hs-amiR-hSHN3*-treated mice (blue, J) while an increase in collagen fibers, calcified matrix, and number of osteoblast-like cells was observed by SEM analysis ($n = 3$/group, K, left and middle). Scale bars, 200 μm (B), 1 mm (H), 100 μm (J), 30 μm (K, left and middle), 2 μm (K, right). A two-tailed unpaired Student's t test for comparing two groups (C and G; error bars, data represent mean ± SD). Representative images of three replicates are displayed (B, E, F, H, J, K).

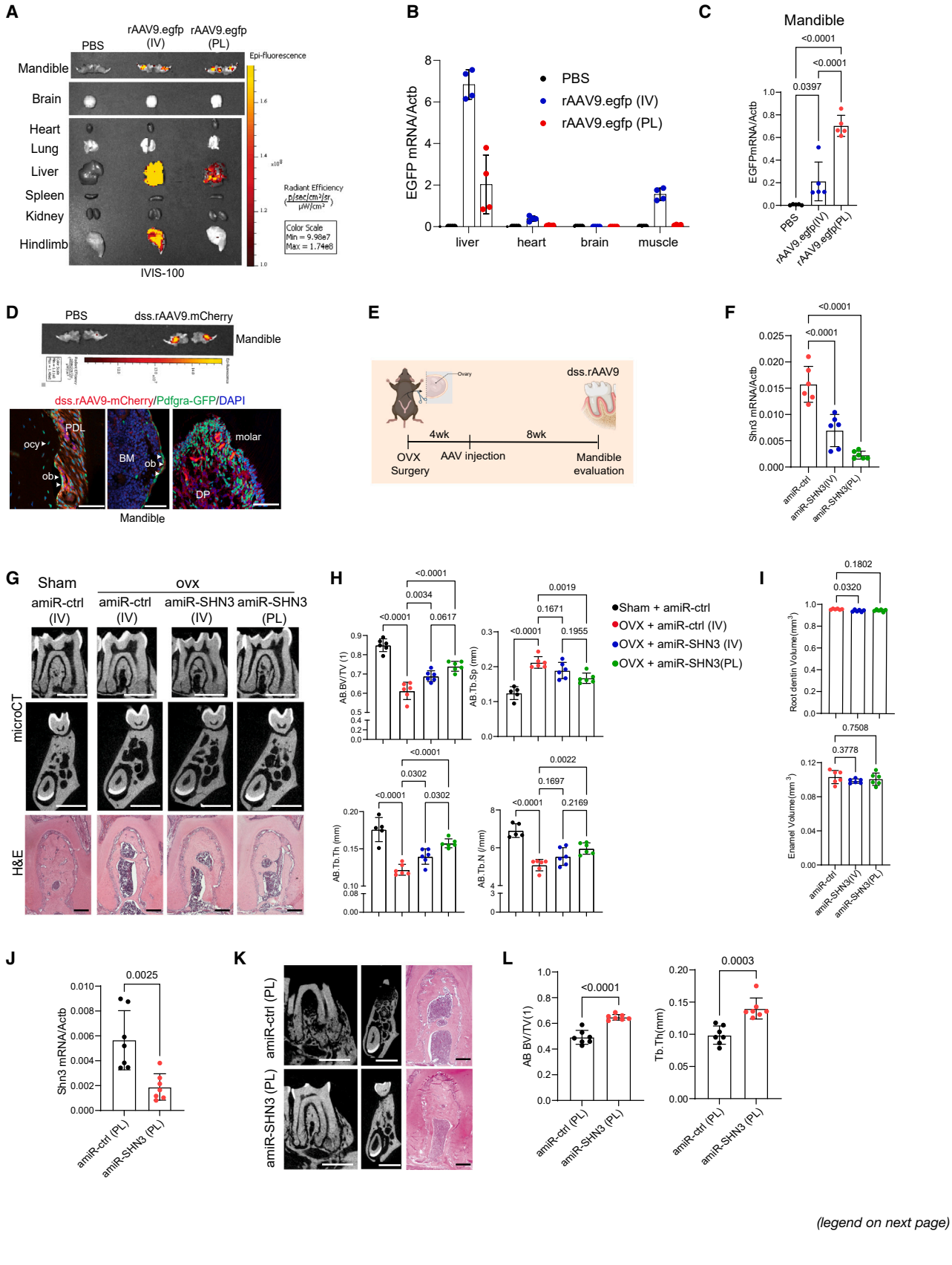

(legend on next page)

Figure S2A, bottom). Sham control or OVX surgery was performed in 12-week-old female mice and 4 weeks later, a single dose of dss.rAAV9 carrying *amiR-ctrl* or *amiR-SHN3* was administered via i.v. or PL injection (Figure 4E). Eight weeks after injection, knockdown efficiency of *Shn3* in AAV-treated OVX mandibles was confirmed by RT-PCR (Figure 4F). While *amiR-ctrl*-treated OVX mice showed a significant reduction in alveolar bone mass compared with sham control mice, this bone loss was reversed by both i.v. and PL injection of *amiR-SHN3*, as shown by increased trabecular BV/TV, thickness, and number and by decreased trabecular space (Figures 4G and 4H). This is consistent with a histological analysis showing a reversal of trabecular bone loss in the bone marrow of *amiR-SHN3*-treated mandible with OVX surgery (Figure 4G, bottom). However, *amiR-SHN3*-treated muscle did not show any changes in myogenic gene expression and microstructures of muscle fibers, suggesting that SHN3 is dispensable of muscle homeostasis (Figures S2E and S2F).

PL injection of dss.rAAV9.*amiR-SHN3* showed greater increase in alveolar bone mass than i.v. injection, demonstrating that local delivery is more effective for AAV transduction and alveolar bone formation than systemic delivery. Notably, unlike genetic deletion of *Shn3*, *amiR-SHN3*-treatment did not increase root dentin volume (Figure 4I). This discrepancy may result from AAV's low silencing efficiency in odontoblasts and osteoblast-lineage cells or AAV injection in older mice that may be too late to promote tooth dentin production.

Next, we examined AAV's ability to restore alveolar bone loss in aging-associated osteoporosis. Twenty-month-old male mice were treated with dss.rAAV9 carrying *amiR-ctrl* or *amiR-SHN3* via PL injection into the mandibular first molar. Two months later, knockdown efficiency of *Shn3* in AAV-treated mandibles was confirmed by RT-PCR (Figure 4J). Compared with *amiR-ctrl*-treated mice, *amiR-SHN3*-treated mice showed a significant increase in alveolar bone mass, as shown by greater BV/TV and Tb.Th (Figure 4K and L). These results demonstrated that bone-targeting AAV-mediated silencing of *Shn3* via PL injection into mandibles is effective in restoring alveolar bone loss in both aging-associated and postmenopausal osteoporosis. Taken together, the approach of local delivery of a SHN3 silencer to mandibles via a bone-targeted AAV may successfully treat alveolar bone loss in osteoporosis.

Liver/heart-"detargeting" AAV-mediated silencing of *Shn3* reverses osteoporosis

Newly developed agents to treat bone loss, such as anti-sclerostin antibody and the small molecule inhibitor of Cathepsin K, have off-target cardiovascular and cerebrovascular events in clinical trials, respectively.[45,46] Thus, AAV's expression in non-skeletal tissues needs to be suppressed. Since dss.rAAV9 can transduce liver and heart, we repressed AAV's expression in liver and heart using liver- and heart-specific miRNA-mediated degradation. The specificity of miR-122 and miR-208a expression in liver and heart was validated by RT-PCR (Figure S3A). Three tandem complementary sites for liver-specific miR-122[47,48] and heart-specific miR-208a[49] (Table S1) were inserted into the 3′ untranslated region (UTR) of the *egfp* reporter gene in the vector genome and then, packaged into dss.rAAV9 capsid (dss.rAAV9.*egfp*.MIR-TS; Figure 5A, top). Eight-week-old mice were i.v. injected with PBS, dss.rAAV9.*egfp*, or dss.rAAV9.*egfp.MIR-TS* and the tissue distribution of AAVs was assessed by EGFP expression using the IVIS optical imaging system (Figure 5B) and fluorescence microscopy on cryo-sectioned tissues (Figure S3B). dss.rAAV9.*egfp*-treated mice showed robust GFP expression in liver, but the expression in dss.rAAV9.*egfp.MIR-TS*-treated liver was markedly reduced. This is consistent with RT-PCR analysis showing a significant decrease in GFP expression in heart and liver treated with dss.rAAV9.*egfp.MIR-TS* relative to dss.rAAV9.*egfp* while the expression was comparable between tibia and muscle (Figure 5C). These results indicate that systemic delivery of dss.rAAV9.egfp.MIR-TS enables GFP expression in the bone, but not in heart, liver, lung, kidney, spleen, and brain.

To examine whether systemic delivery of dss.rAAV9.*amiR-Shn3.MIR-TS* can reverse femoral bone loss in postmenopausal osteoporosis, a single dose of dss.rAAV9 carrying *amiR-ctrl*, *amiR-SHN3*, or *amiR-SHN3.MIR-TS* was i.v. injected into 12-week-old female mice 4 weeks after sham control or OVX surgery. Eight weeks later, knockdown efficiency of *Shn3* in AAV-treated OVX tibia was

Figure 4. AAV-mediated silencing of SHN3 reverses alveolar bone loss in osteoporotic mice

(A–C) Two-month-old mice were treated with PBS or rAAV9.*egfp* via intravenous (i.v., 2.5×10^{13}vg/kg) injection or periodontal ligament (PL, 2.5×10^{12} vg/kg) injection into the mandibular first molar. Ten days later, EGFP expression in individual tissues was monitored by IVIS-100 optical imaging (A) and RT-PCR (n = 4–5/group, B, C). (D) Two-month-old *Pdgfrα-GFP* reporter mice were treated with PBS or dss.rAAV9.*mCherry* (2.5×10^{12} vg/kg) via PL injection to visualize AAV-transduced Pdgfrα-lineage cells in the alveolar bone (n = 3/group). Ten days later, mCherry expression in mandibles was monitored by IVIS-100 optical imaging (top) and fluorescence microscopy on cryo-sectioned mandibles (bottom). PDL: periodontal ligament, BM: bone marrow, DP: dental pulp, ob: osteoblast, ocy: osteocyte. Scale bar, 50 μm. (E–I) Diagram of the study and treatment methods. Sham or OVX surgery was performed on 3-month-old female mice and 4 weeks later, mice were treated with dss.rAAV9 carrying *amiR-ctrl* or *amiR-SHN3* via i.v. (2.5×10^{13} vg/kg) injection or PL (2.5×10^{12} vg/kg) injection (E). Eight weeks later, *Shn3* mRNA expression in the mandible was assessed by RT-PCR (n = 6/group, F). 2D microCT images (G, top and middle) and relative quantification (H) and H&E staining (G, bottom), showing an increase in alveolar bone mass (n = 6/group) in the *amiR-SHN3*-treated OVX mice. MicroCT analysis showing root dentin and enamel volume of mandibular first molar (n = 6/group, I). (J and K) Twenty-month-old male mice were treated with dss.rAAV9 carrying *amiR-ctrl* or *amiR-SHN3* (2.5×10^{12} vg/kg) via PL injection and 8 weeks later, *Shn3* mRNA expression in the mandible was assessed by RT-PCR (n = 7/group, J). 2D microCT images (K, left and middle) and relative quantification (L) and H&E staining (K, right), showing an increase in alveolar bone mass (n = 7/group) in the *amiR-SHN3* treated mice. Scale bars, 100 μm (D; G, bottom; K, right), 1 mm (G, top and middle; K, left and middle). A two-tailed unpaired Student's t test for comparing two groups (J and L) or ordinary one-way ANOVA with Dunnett's multiple comparisons test (B, C, F, H, I). (B), (C), (F), (H)–(K), data represent mean ± SD. Representative images are displayed (A, D, G, K).

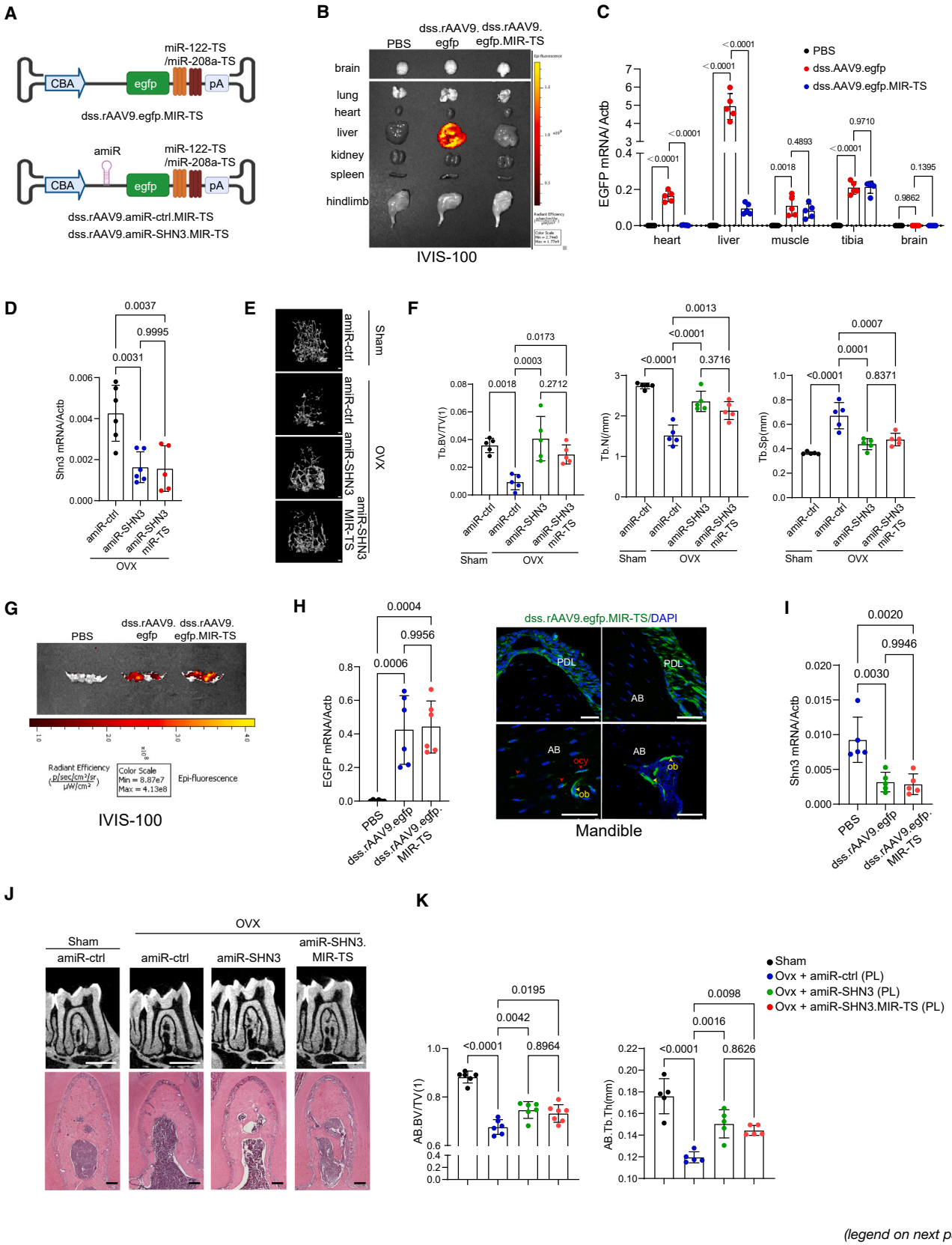

(legend on next page)

confirmed (Figure 5D). While *amiR-ctrl*-treated OVX mice showed significant reductions in femoral bone mass compared with sham control mice, this bone loss was reversed by both *amiR-SHN3* and *amiR-SHN3.MIR-TS*, as shown by increased trabecular BV/TV, thickness, and number and decreased trabecular space (Figures 5E and 5F). Thus, miR-122- and miR-208a-mediated repression effectively "detargets" AAV expression in liver and heart without affecting anabolic bone increase by *amiR-SHN3*.

Next, we compared EGFP expression in the alveolar bone treated with dss.rAAV9.*egfp* and dss.rAAV9.*egfp.MIR-TS* via local delivery. Eight-week-old mice were treated with dss.rAAV9.*egfp* or dss.rAAV9.*egfp.MIR-TS* via PL injection into the mandibular first molar. Ten days later, EGFP expression in the mandible was assessed by IVIS optical imaging, RT-PCR, and fluorescence microscopy (Figures 5G and 5H), demonstrating equivalent expression levels in AAV-treated mandibles. Similar to dss.rAAV9.*egfp*, dss.rAAV9.*egfp.MIR-TS* effectively transduced a subset of PL cells and osteoblast-lineage cells within alveolar bone. Thus, PL injection of dss.rAAV9.*MIR-TS* to the mandible may be a safe and effective strategy to target alveolar bone.

To compare the therapeutic efficacy of dss.rAAV9.*amiR-SHN3* vs. dss.rAAV9.*amiR-SHN3.MIR-TS* in osteoporotic alveolar bone, 12-week-old female mice were treated with the AAVs via PL injection to the mandibular first molar 4 weeks after sham control or OVX surgery (Figure S3C). Eight weeks later, knockdown efficiency of *Shn3* in AAV-treated OVX mandible was confirmed by RT-PCR (Figure 5I). While *amiR-ctrl*-treated OVX mice showed a significant reduction in alveolar bone mass compared with sham control mice, this bone loss was reversed by both *amiR-SHN3.MIR-TS* and *amiR-SHN3*, as shown by increased trabecular BV/TV and thickness (Figures 5J and 5K). Thus, PL injection of dss.rAAV9.*amiR-SHN3.MIR-TS* effectively restores alveolar bone loss in postmenopausal osteoporosis while securing AAV's expression in mandibles. We conclude that silencing of *Shn3* in mandibles via a bone-targeted AAV with bone-specific tropism (dss.rAAV9 capsid) and liver- and heart-detargeting capability (miR-122/miR-208a-mediated repression) is a targeted and safe approach to restore alveolar bone loss in osteoporosis.

Vibration-inducible expression of bone-targeted AAV in mandibles

Alveolar bone continuously receives mechanical stimuli, such as chewing, biting, and speaking, which is crucial to maintain alveolar bone mass.[4] Given that WNT signaling is a major mechano-sensing pathway in osteoblast-lineage cells to promote bone formation,[50] activation of WNT signaling in the alveolar bone was examined using transgenic TCF/Lef1-GFP reporter mice that express a fused protein of histone 2B and GFP in response to WNT stimulation.[51] Fluorescence microscopy showed GFP expression in multiple cell populations within alveolar bone, including PL cells, odontoblasts, osteoblasts, and osteocytes (Figure 6A). These results indicate robust WNT signaling in alveolar bone-residing cells. Notably, compared with skull bone requiring low mechanical demands, mandible and tibia that require high mechanical demands showed elevated expression of WNT-responsive genes, *Axin2* and *Lef-1* (Figure 6B), suggesting that WNT signaling in mandibles is activated in response to mechanical stress.

Upon WNT stimulation, the key transcription factor β-Catenin is released from the degradation complex and forms a protein complex with other transcription factors, TCF and LEF-1, in the nucleus, resulting in transcriptional activation.[52] To assess mechanical stress-induced activation of WNT signaling in alveolar bone, we generated the dss.rAAV9 that expresses GFP protein under the control of the LEF-1/TCF-responsive promoter (dss.rAAV9.pLef/Tcf-*egfp*, Figure 6C). Calvarial osteoblasts (COBs) were treated with dss.rAAV9.pLef/Tcf-*egfp* and then stimulated with a recombinant Wnt3a (rWnt3a) ligand or flow stress. GFP expression (fluorescence microscopy, Figure 6D) and mRNA expression of *egfp*, *Axin2,* and *Lef-1* (RT-PCR, Figures 6E and S4A) in AAV-treated COBs were markedly upregulated in response to rWnt3a or flow stress. These results demonstrate the ability of dss.rAAV9.pLef/Tcf-*egfp* to induce GFP expression in response to mechanical stress via WNT signaling activation.

Previous studies demonstrated that high-frequency vibration (HFV) treatment shows promise in dental practice to enhance alveolar bone density and fibroblast stimulation within the PL.[53–55] Since HFV activates WNT signaling as a mechanical stress,[56] we tested

Figure 5. Liver/heart-detargeting AAV-mediated silencing of SHN3 reverses bone loss in osteoporotic mice

(A) Diagram of the liver and heart-detargeting AAV vector construct containing an *egfp*, *amiR-ctrl*, or *amiR-SHN3*. Target sequences of the liver-abundant miR-122 and the heart-abundant miR-208a were inserted into the 3′UTR of *egfp* to repress transgene expression. (B and C) 2-month-old mice were treated with PBS, dss.rAAV9.*egfp*, or dss.rAAV9.*egfp.MIR-TS* (2.5×10^{13} vg/kg) via i.v. injection and 10 days later, EGFP expression in individual tissues was assessed by IVIS-100 optical imaging (B) and RT-PCR (C). (D–F) Sham or OVX surgery was performed on 3-month-old female mice and 4 weeks later, mice were treated with dss.rAAV9 carrying *amiR-ctrl*, *amiR-SHN3,* or *amiR-shn3-MIR-TS* (2.5×10^{13} vg/kg) via i.v. injection. Eight weeks later, *Shn3* mRNA expression in the tibia was assessed by RT-PCR (n = 5–6/group, D). Femoral bone mass was assessed by microCT. 3D microCT images (E) and relative quantification (F) are displayed (n = 5/group). Tb.BV/TV: trabecular bone volume per tissue volume, Tb.N: trabecular number, Tb.Sp: trabecular space. (G and H) Two-month-old mice were treated with PBS, dss.rAAV9.*egfp*, or dss.rAAV9.*egfp.MIR-TS* (2.5×10^{12} vg/kg) via PL injection into the mandibular first molar. Ten days later, EGFP expression in the mandible was assessed by IVIS-100 optical imaging (G), RT-PCR (n = 6/group, H, left), and fluorescence microscopy on cryo-sectioned mandible (H, right). (I–K) Sham or OVX surgery was performed on 3-month-old female mice and 4 weeks later, mice were treated with dss.rAAV9 carrying *amiR-ctrl*, *amiR-SHN3,* or *amiR-SHN3.MIR-TS* (2.5×10^{12} vg/kg) via PL injection. Eight weeks later, *Shn3* mRNA expression in the mandible was assessed by RT-PCR (n = 5/group, I). 2D microCT images (J, top) and relative quantification (n = 5–7/group, K) and H&E staining (J, bottom) show a reversal of alveolar bone loss in OVX mandible. Scale bars, top, 1 mm (E; J, top); 100 μm (H; J, bottom). Ordinary one-way ANOVA with Dunnett's multiple comparisons test (C, D, F, H, I, K; data represent mean ± SD). Representative images of five (B; E, left) or six (G; H, right; J) replicates are displayed.

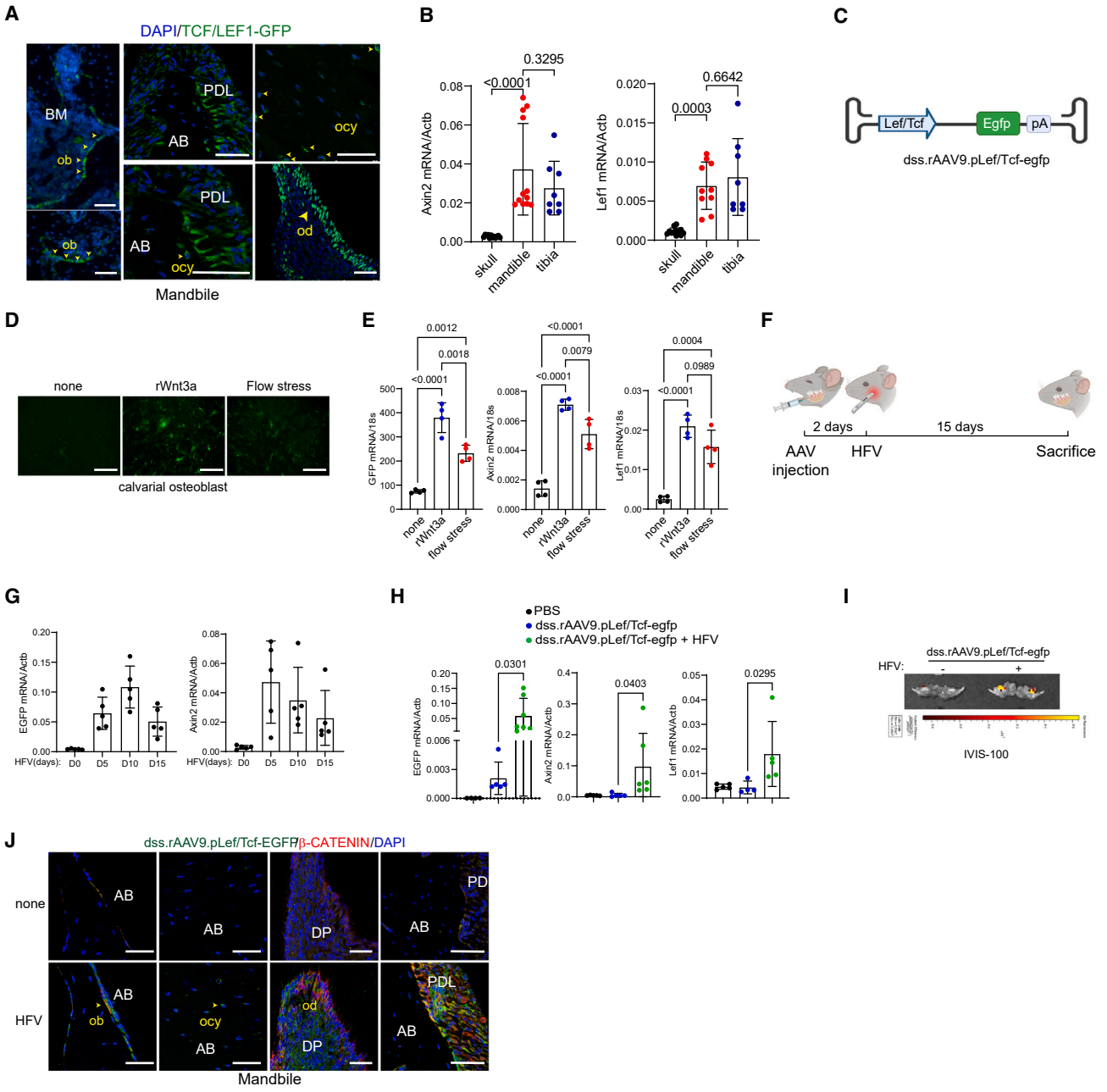

Figure 6. Development of a bone-targeting AAV with vibration-inducible expression

(A) Fluorescence microscopy was performed on cryo-sectioned mandibles of 2-month-old TCF/Lef1-HIST1:H2BB/EGFP reporter mice to locate cells with WNT signaling activation in the alveolar bone.

(B) mRNA expression of WNT-responsive genes, *Axin2* and *Lef1*, in the calvaria, mandible, and tibia of 2-month-old mice (n = 8–10/group).

(C) The AAV vector genome containing the LEF/TCF promoter (pLef/Tcf) and *egfp* reporter gene was packaged into the dss.rAAV9 capsid. (D and E) Calvarial osteoblasts (COB) were transduced with dss.rAAV9.pLef/Tcf-*egfp* (4 x 10^6 vg/cell) and stimulated with a recombinant WNT3a or flow stress. EGFP expression was assessed by fluorescence microscopy (D) and RT-PCR (n = 4/group, E). WNT signaling activity was assessed by measuring mRNA expression of *Axin2* and *Lef1* (n = 4/group, E). (F–J) Diagram of the study and treatment methods. Two-month-old mice were treated with dss.rAAV9.pLef/Tcf-*egfp* (2.5 × 10^{12} vg/kg) via PL injection into the mandibular first molar and 2 days later, the mandible was stimulated daily with HFV treatment for up to 15 days (F). RNA was isolated from the treated mandible at days 0, 5, 10, and 15 post-treatment. mRNA expression of *egfp* and *Axin2* was assessed by RT-PCR (n = 5–7/group, G). AAV-treated mandible was stimulated daily with or without HFV treatment for

(legend continued on next page)

whether HFV treatment can induce GFP expression in dss.rAAV9.pLef/Tcf-*egfp*-treated mandibles via WNT signaling activation. Two days after PL injection into the mandibular first molar, 8-week-old mice were treated daily with HFV (200 Hz, 30 s) on the mandible (Figure 6F). Of note, HFV did not induce any adverse effects on tooth, gum, skull, and mandible structures (Figures S4B–S4D). Expression of *egfp* and *Axin2* in the mandible was assessed by RT-PCR at different time points, demonstrating that their expression in the mandible peaked at both 10 and 5 days of daily HFV stimulation, respectively (Figure 6G). Compared with no HFV or PBS treatment, 10 days of HFV treatment significantly increased the expression of *egfp, Axin2,* and *Lef1* in the mandible (Figure 6H). Notably, HFV-induced expression of *egfp* in AAV-treated mandible corresponds to WNT-responsive expression of *Axin2* and *Lef1* (Figure S6A). The IVIS optical imaging system confirmed that GFP expression in AAV-treated mandible was detected only in the presence of HFV stimulation (Figure 6I). AAV-treated liver also showed modest expression of GFP proteins, but the expression was markedly reduced upon HFV stimulation. There was little to no expression in brain, heart, lung, kidney, and spleen regardless of HFV stimulation (Figure S5). Within alveolar bone, a subset of β-Catenin-expressing cells, including PLs, osteoblasts, osteocytes, and odontoblasts expressed GFP proteins (Figure 6J). These results suggest that PL injection of dss.rAAV9.pLef/Tcf to mandibles enables control of transgene expression in alveolar bone in response to HFV stimulation.

Vibration-inducible AAV gene therapy reverses alveolar bone loss in osteoporosis

In a previous study, SHN3 deficiency upregulated *Sost* expression among known WNT antagonists and inhibition of both factors further increased WNT/β-catenin signaling in osteoblast-lineage cells, suggesting that expression of SHN3 and SOST is connected via a negative feedback mechanism.[57] Thus, we generated a bone-targeted AAV that confers HFV-induced single silencing of *Shn3* as a moderate WNT signaling activator (dss.rAAV9.pLef/Tcf.*amiR-SHN3*) and dual silencing of *Shn3* and *Sost* as a strong WNT signaling activator (dss.rAAV9.pLef/Tcf.*amiR-SHN3/SOST)* (Figure S6B). Four weeks after sham control or OVX surgery, 12-week-old female mice were treated with dss.rAAV9.pLef/Tcf carrying *amiR-ctrl*, *amiR-SHN3*, or *amiR-SHN3/SOST* via PL injection to the mandibular first molar and then stimulated daily with HFV for 10 days (Figure S6C). HFV stimulation of *amiR-SHN3*-treated mandibles led to a decrease in *Shn3* expression and an increase in *Lef-1* and *Axin2* expression and these mandibles did not show any decrease in *Shn3* expression in the absence of HFV stimulation (Figures 7A and 7B). In *amiR-SHN3/SOST*-treated mandibles, HFV stimulation further upregulated *Lef1* and *Axin2* expression by silencing both *Shn3* and *Sost* expression (Figures 7C and 7D). These results demonstrate that HFV stimulation of AAV-treated mandibles effectively silenced the expression of *Shn3* and/or *Sost* and activated WNT signaling.

Regardless of HFV stimulation, *amiR-ctrl*-treated OVX mice showed a significant decrease in bone formation rate (BFR) and mineral apposition rate (MAR) in the alveolar bone, demonstrating reduced osteoblast activity *in vivo* (Figure 7E). By contrast, HFV stimulation of *amiR-SHN3/SOST*-treated mandibles led to nearly complete reversal of the BFR and MAR while only the modest increase was seen in *amiR-SHN3*-treated mandibles (Figure 7E). MicroCT analysis of *amiR-SHN3/SOST*-treated mandibles also showed an increase in trabecular BV/TV and thickness and a decrease in trabecular space when treated with HFV. Unlike the CBA promoter-driven silencing of *Shn3* showing a significant increase in alveolar bone mass, only a modest increase in bone mass was observed under the LEF-1/TCF promoter-driven silencing after HFV treatment (Figures 7F and 7G). This was consistent with the RT-PCR data showing that compared with control treatment, the CBA promoter-driven silencing of *Shn3* resulted in high GFP expression, robust knockdown of *Shn3*, and increased expression of the osteogenic gene alkaline phosphatase (Alp) regardless of HFV stimulation. However, HFV-induced silencing of *Shn3* under the LEF-1/TCF promoter led to a modest increase in *Egfp* and *Alp* expression along with a modest knockdown of *Shn3* (Figure S7), resulting in weak osteogenesis. These results suggest that HFV-induced dual silencing of *Shn3* and *Sost* is more effective than single silencing of *Shn3* in enhancing WNT signaling and osteoblast activity and promoting alveolar bone formation in postmenopausal osteoporosis. Notably, *amiR-SHN3/SOST*-treated mandibles did not show any change in dentin deposition rates after HFV stimulation, demonstrating that HFV-induced dual silencing of *Shn3* and *Sost* in the mandible does not affect tooth dentin production (Figures S6D and S6E).

A previous study has shown that hyperactivation of WNT/β-Catenin signaling in osteoblasts inhibits osteoclast development via upregulated production of osteoprotegerin (OPG).[58] Accordingly, HFV stimulation of *amiR-SHN3/SOST*-treated mandibles upregulated *Opg* expression while the expression was not affected by *amiR-SHN3* treatment (Figure 7H). Compared with sham control mandibles, *amiR-ctrl*-treated OVX mandibles showed a significant increase in osteoclast development, as shown by an increase in tartrate-resistant acid phosphatase (*Trap, Acp5*) mRNA expression and TRAP-positive osteoclast numbers on alveolar bone surface. This increase was reversed by *amiR-SHN3/SOST* treatment, but not by *amiR-SHN3* treatment, in the presence of HFV stimulation (Figures 7I–7K). These results show that HFV-induced dual silencing of *Shn3* and *Sost* in the mandible hyperactivates WNT/β-Catenin signaling in osteoblasts and inhibits osteoclast-mediated bone resorption via upregulation of OPG expression. However, HFV-induced single

10 days and WNT signaling activity was assessed by mRNA expression of *egfp*, *Axin2,* and *Lef1* (n = 4–6/group, H), IVIS-100 optical imaging (I), and fluorescence microscopy on cryo-sectioned mandible (J). AAV-treated mandible was stained with β-Catenin, demonstrating that EGFP expression in β-Catenin^{high} cells was upregulated by HFV treatment (J). Scale bar, 50 μm (A and J), 100 μm (D). Ordinary one-way ANOVA with Dunnett's multiple comparisons test (B, E, G, H; data represent mean ± SD). Representative images of three (A, J), four (D), or six (I) are displayed (A, D, I, J).

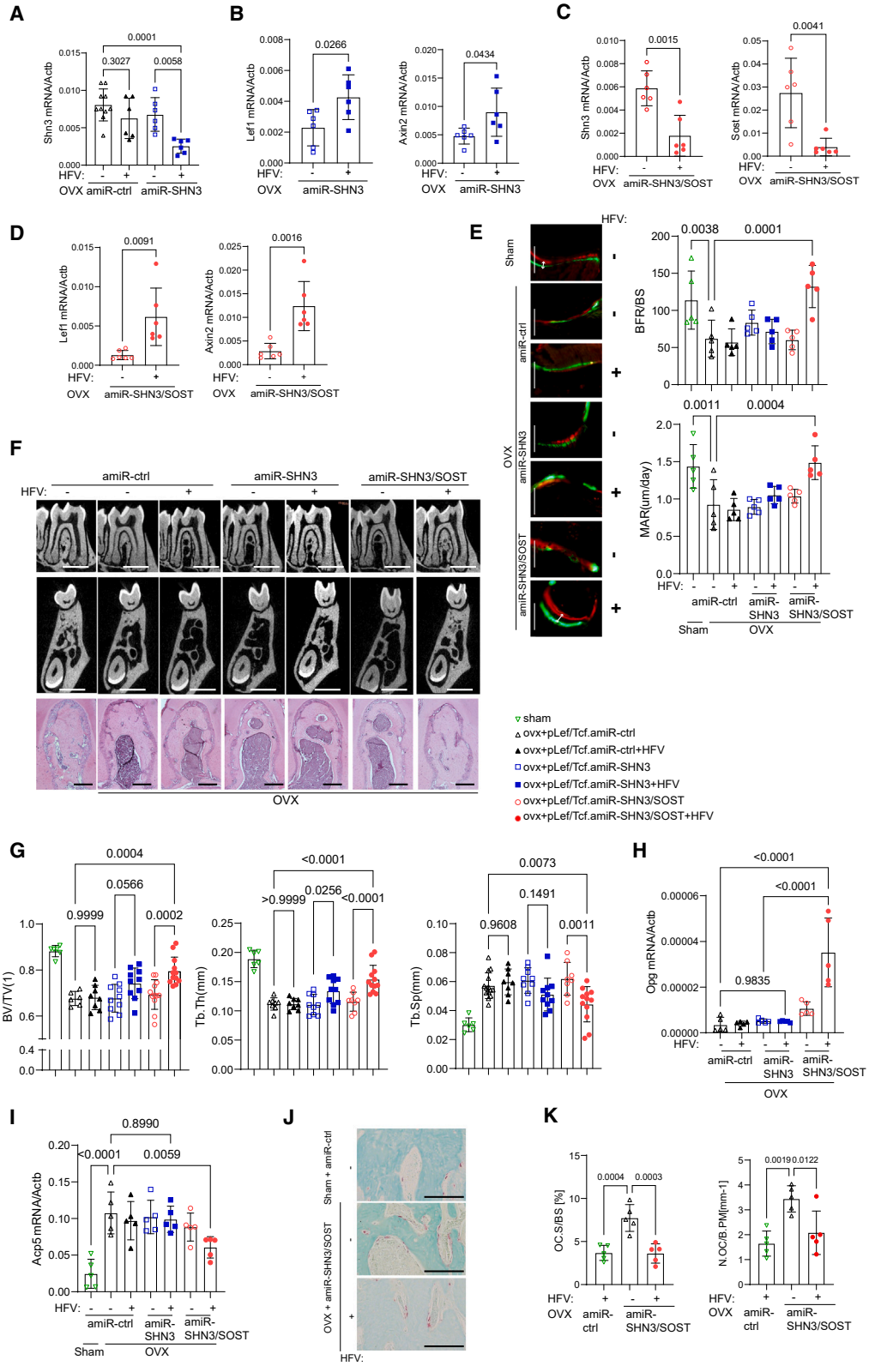

(legend on next page)

silencing of *Shn3* shows a modest increase on WNT signaling without affecting OPG expression and osteoclast development. Taken together, activation of WNT signaling in mandibles via SHN3 and/or SOST knockdown using the bone-targeted AAV with liver/heart-detargeting capability or HFV-induced expression could be a promising, safe, and targeted therapeutic option to restore alveolar bone loss in osteoporosis.

DISCUSSION

Alveolar bone loss results from various pathological events, such as osteoporosis, periodontal disease, surgical excision, cranioplasty, infection, congenital malformations, and oral cancer,[59] which can significantly affect the quality of life of patients. However, there are key hurdles to developing effective treatments for alveolar bone loss. First, the unique microenvironment and anatomical complexity of the alveolar bone create obstacles in drug delivery, as its densely mineralized composition restricts drug penetration and distribution.[60] Additionally, the surrounding soft tissues, such as periodontal ligaments and gingiva, also hinder drug accessibility. Second, the limited regenerative potential of the alveolar bone hampers efforts to stimulate bone formation and repair. Finally, overcoming the dynamic nature of the oral cavity, which exposes the alveolar bone to various physiological and mechanical forces, is essential for ensuring drug stability, bioavailability, and efficacy.[61,62] Currently, bone grafting is considered a primary solution to re-establish the morphology of alveolar bone. However, it is unable to restore the functional needs of alveolar bone and causes potential postoperative complications.

AAV-mediated gene therapy offers a potential treatment option for various skeletal diseases with target specificity of a disease-cause gene and long-lasting therapeutic effectiveness.[63] As expression of the osteogenic suppressor SHN3 is highly upregulated in jaw bones with osteoporosis, AAV-mediated silencing of *Shn3* expression in osteoblasts via systemic or local delivery to jaw bone effectively enhanced osteoblast activity, promoted bone regeneration, and restored alveolar bone loss in osteoporosis. Moreover, our AAV gene therapy can avoid untoward off-target adverse effects in non-related organs, such as liver, heart, brain, lung, spleen, kidney, and skeletal muscle, by improving bone-specific tropism and expression using a bone-targeted capsid and tissue-specific miRNA-mediated detargeting of liver and heart, respectively. Finally, since jawbone is a mechanical sensing tissue that requires constant mechanical stress to maintain alveolar bone mass, topical HFV treatment restored alveolar bone loss in osteoporotic mice treated with our vibration-inducible AAV without any side effects. Thus, our bone anabolic AAV gene therapy provides a non-invasive, safe, and targeted approach for the treatment of alveolar bone loss, which can be easily applicable to clinical settings.

SHN3 is a large zinc-finger protein that functions as a potent endogenous inhibitor of bone formation.[31,28] SHN3 controls the stabilization of β-Catenin in osteoblasts via regulation of the ERK MAPK pathway and its deletion augments osteoblast function by enhancing WNT signaling.[27] SHN3-deficient mice displayed a progressive increase in lamellar bone production of long bone and vertebrae without any abnormalities in non-skeletal tissues.[31] We also found a significant increase in alveolar bone mass and tooth dentin volume in these mice. Thus, these properties together make SHN3 inhibition an attractive approach to restore bone loss in osteoporosis. However, current drug modalities, such as small compounds and biological antibodies, are not effective for SHN3 inhibition as SHN3 is an intracellular, non-enzymatic, adaptor protein.

A modest 30% reduction of *Shn3* mRNA levels with postnatal induction of a transgenic shRNA results in >40% increase in relative trabecular bone mass,[64] suggesting knockdown of *Shn3* mRNA is an alternative approach to inhibit SHN3 in bone. For bone-specific silencing of *Shn3* expression, we used a bone-targeted AAV capsid where a bone-homing $(AspSerSer)_6$ peptide motif was grafted onto an AAV9-VP2 capsid protein (dss.rAAV9).[26,41] In our previous studies, short hairpin RNA (shRNA) cassettes in the AAV vector genome hindered and redirected rAAV genome replication, leading to heterogeneous populations comprising a mixture of full-length genomes and truncated vector species that lack the capacity to silence mRNAs.[39] Additionally, overexpression of shRNAs induces cytotoxicity in mammalian cells by perturbing RNA interference machinery or exhibiting significant off-target silencing.[65,66] Therefore, we used an AAV-compatible SHN3 silencer (*amiR-SHN3, hs-amiR-SHN3, hs-amiR-hSHN3*). This strategy enables efficient gene knockdown, increases vector genome integrity, and limits shRNA-related toxicity, while reducing off-target silencing 10-fold compared with conventional shRNA constructs.[38,67] Finally, since a bone-targeted AAV capsid still shows modest transduction to heart and liver, we repressed AAV's expression in these tissues using miR-208a (heart) and miR-122 (liver)-mediated degradation (dss.rAAV9.*MIR-TS*). Systemic delivery of dss.rAAV9.*MIR-TS.amiR-SHN3* proved effective

Figure 7. Vibration-inducible AAV-mediated silencing of SHN3/SOST reverses alveolar bone loss in osteoporotic mice

(A–K) Sham or OVX surgery was performed on 3-month-old female mice and 4 weeks later, mice were treated with dss.rAAV9.pLef/Tcf carrying *amiR-ctrl*, *amiR-SHN3*, or *amiR-SOST/SHN3* (2.5×10^{12} vg/kg) via PL injection to the mandibular first molar. Two days later, AAV-treated mandibles were stimulated daily with HFV treatment for 10 days. Seven weeks later, mRNA expression of *Shn3* and *Sost* in the mandible was assessed by RT-PCR (n = 6–10/group, A and C). WNT signaling activity was assessed by measuring mRNA expression of *Axin2* and *Lef1* (n = 6/group, B and D). Calcein/alizarin red labeling images and relative histomorphometric quantification of BFR/BS and MAR are displayed (n = 5/group, E). BFR/BS, bone formation rate/bone surface; MAR, mineral apposition rate. 2D microCT images (F, top and middle) and relative quantification (n = 6–12/group, G) and H&E staining (F, bottom) of alveolar bone are displayed. *amiR-SOST/SHN3* treatment upregulated mRNA expression of *Osteoprotegerin (Opg)* in HFV-treated mandibles (H). Osteoclast development in AAV-treated mandibles was assessed by measuring *Trap* mRNA expression (I) and numbers of TRAP-positive osteoclasts on the surface of alveolar bone (n = 5/group, J and K). Oc.S/BS: osteoclast surface/bone surface; N.Oc/B.pm: osteoclast number/Bone perimeter. Scale bars, 200 μm (E), 1 mm (F, top and middle), 100 μm (F, bottom). A two-tailed unpaired Student's t test for comparing two groups (B, C, D) or ordinary one-way ANOVA with Dunnett's multiple comparisons test (A, E, G, H, I, K). (A)–(E), (G), (H), (I), (K): data represent mean ± SD. Representative images are displayed (E, F, I).

in reversing bone loss at two different anatomical locations (alveolar bone and long bone) in a mouse model for postmenopausal osteoporosis. In particular, its ability to restore alveolar bone loss in osteoporotic mice was markedly improved when locally delivered to the mandibular first molar via PL injection. Thus, local delivery of our bone-targeted AAV with liver/heart-detargeting capability can offer mandible-specific knockdown of *Shn3* to restore alveolar bone loss in osteoporosis. Further investigation of these therapies will need to evaluate the long-term durability of *Shn3* silencing, as long-term suppression of alveolar bone loss will be necessary to treat osteoporosis patients.

Precise spatiotemporal control of AAV-mediated silencing of *Shn3* can provide a targeted drug modality that reverses alveolar bone loss in osteoporosis while limiting untoward side effects in nonrelated organs. Alveolar bone continuously receives mechanical stimuli, which activates bone-forming WNT signaling. As a mechanical stimulation, HFV treatment shows promise in dental practice to accelerate orthodontic tooth movement by enhancing surrounding bone density and fibroblast stimulation within the periodontal ligament.[53–55] However, its bone-forming effects are limited to healthy conditions as HFV treatment can also trigger osteoclast-mediated bone resorption under pathological conditions, such as osteoporosis and periodontitis.[68] Thus, we engineered a bone-targeted AAV that can promote bone formation and inhibit bone resorption simultaneously in response to HFV stimulation. HFV-induced dual silencing of two WNT antagonists, SHN3 and SOST, in the mandible of osteoporotic mice hyperactivates canonical WNT signaling and enhances osteoblast development in alveolar bone while suppressing osteoclast development via elevated OPG production. However, HFV-induced single silencing of SHN3 had a minimal effect in osteoporotic alveolar bone. Unlike the chicken-β-actin promoter, HFV-induced expression of *amiR-SHN3* under the control of the LEF-1/TCF-responsive promoter may not be sufficient to confer robust knockdown of *Shn3* expression and increase osteoblast activity.

In summary, we developed a targeted and safe, bone anabolic gene therapy to restore alveolar bone loss in osteoporosis. Local delivery of a bone-targeted AAV with liver/heart-detargeting capability or HFV-induced expression selectively silenced SHN3 and/or SOST expression in mandibles and restored alveolar bone loss in osteoporotic mice. The potential of the bone-targeted AAV-mediated therapy also extends beyond osteoporosis to periodontitis, surgical excision, cranioplasty, infection, congenital malformations, and oral cancer, where the ability of AAV-delivered payloads can restore the functional needs of alveolar bone. Future investigation for vector biodistribution, toxicity, dose range, and therapeutic efficacy in non-human primates is required before any consideration can be given to applying AAV gene therapy to individuals with alveolar bone loss.

MATERIALS AND METHODS

Cell culture and reagents

Human bone marrow-derived mesenchymal stromal cells (BMSCs, #7500) were purchased from ScienCell Research Laboratories and cultured according to the manufacturer's manuals. Human periodontal ligament stem cells (PDLSCs, 36085-01) were purchased from Celprogen and cultured in the human PDLSCs complete growth media with serum (M36085-01S) for maintenance or cultured in the human PDLSC culture differentiation media with serum (M36085-01DS) for osteogenic differentiation. Mouse alveolar bone-marrow-derived MSCs were isolated from 1-month-old $Shn3^{Pdgfr\alpha}$ and $Shn3^{fl/fl}$ mandibles as described previously.[69] Briefly, mandibular bones were collected and processed by removing attached soft tissues and teeth, including molars and incisors. Cells were then obtained using a digestion solution that contains collagenase type I (Worthington Biochem, LS004196) and dispase II (Roche,10165859001). The resulting cell suspensions were filtered (40 μm) and washed using PBS and maintained in α-MEM (Gibco). Mouse COBs were isolated from the calvaria of wild-type neonates at postnatal day 3 (C57BL/6J). Cells were maintained in α-MEM (Gibco) containing 10% FBS (Corning), 2 mM L-glutamine (Corning), 1% penicillin/streptomycin (Corning), and 1% nonessential amino acids (Corning) while they were differentiated into mature osteoblasts under osteogenic medium containing ascorbic acid (200 μM, Sigma, #A8960) and β-glycerophosphate (10 mM, Sigma, #G9422). Recombinant WNT3a was purchased from R&D systems (#1324-WN).

rAAV vector design and production

Bone-targeting AAV9 capsid (dss.rAAV9) was generated as described in previous studies.[40,70] Mouse or human miR-33 scaffold design rules were applied to generate optimized artificial miRNA (amiR) cassettes and amiR target sequences were designed using a custom Excel macro and cloned into a self-complementary AAV vector genome. Plasmids were constructed by Gibson assembly and standard molecular biology methods. Validated DNA sequences for *amiR-ctrl*, *amiR-SHN3, hs-amiR-SHN3,* and *amiR-SOST/SHN3* were synthesized as gBlocks, cloned into the intronic region of the pAAVsc-*CB6-Egfp* plasmid at the restriction enzyme sites (PstI and BglII).[71] To generate a liver- and heart-detargeting AAV (**dss.rAAV9.*egfp*.MIR-TS**), endogenous complementary sequences for miR-122 and miR-208a were synthesized as gBlocks and inserted into the 3′UTR of the *egfp* reporter gene in the pAAVsc-*CB6-Egfp* plasmid and packaged into the dss.AAV9 capsid. To generate a mechanical stress-inducible AAV (**dss.rAAV9.pLef/Tcf-*egfp***), DNA sequences for the TCF/LEF promoter (pTcf/Lef) adapted from the M50 super 8x TopFlash reporter gene (Addgene, #12456) were synthesized as gBlocks and then replaced the *CB6* promoter of the pAAVsc-*CB6-Egfp* plasmid. Constructs were verified by sequencing and then packaged into the dss.rAAV9 capsid. rAAV9 production was executed by transient transfection in HEK293 cells, purified by CsCl sedimentation, and quantified by droplet digital PCR (ddPCR) on a QX200 ddPCR system (Bio-Rad) using the *Egfp* or *mCherry* prime/probe set. The sequences of gBlocks and oligonucleotides for ddPCR are listed in Table S1.

Quantitative RT-PCR analysis

Total RNA was purified from cells using QIAzol (QIAGEN) and cDNA was synthesized using the High-Capacity cDNA Reverse Transcription Kit from Applied Biosystems. Quantitative RT-PCR was

performed using SYBR Green PCR Master Mix (Bio-Rad) with the CFX connect RT-PCR detection system (Bio-Rad). To measure *Shn3* mRNA levels in bone tissues, after removal of bone marrow, soft tissue, and teeth, including molars and incisors, mandibles or tibias were snap-frozen in liquid nitrogen for 30 s and in turn, homogenized in 1 mL of QIAzol for 1 min. Alternatively, a TaqMan miRNA assay kit (Applied Biosystems) was used to measure the expression of miR-122 and miR-208a. miRNAs were isolated from the mandible, liver, or heart using the mirVana miRNA isolation kit (Ambion), followed by cDNA synthesis using the TaqMan miRNA reverse transcription kit (Applied Biosystems). The cDNA was used for RT-PCR using a TaqMan miRNA assay kit (Applied Biosystems) according to the manufacturer's protocol: miR-122-5p (assay ID: 002245), miR-208a-3p (assay ID: 000511). Primers used for PCR are described in Table S1.

Human subjects and analysis

Four de-identified alveolar bone samples were obtained from young (20–25-year-old) and aged (older than 60 years old) patients at the School of Stomatology Wuhan University during dental implant surgery. Total RNAs were extracted from alveolar bone areas and mRNA expression of *SOST, DKK1*, and *SHN3* was examined by RT-PCR. These were obtained under institutional review board approval (Protocol #: 2022D03).

Mice

Mice were housed in a constant environment (up to five mice per cage), ambient temperature of 21 ± 2 °C, circulating air, and constant humidity of 50% ± 10%, in a 12-h light, 12-h dark cycle. Mice were given a standard mouse chow diet and monitored every 3 days for the amount of their food and water intake and signs of distress. For signs of severe distress, including general malaise, severe cachexia, or more than 20% loss of body weight, humane euthanasia was performed in consultation with veterinary staff. Mice were euthanized in a carbon dioxide chamber, followed by cervical dislocation. Neonates were euthanized by decapitation. Cre deleter mice (C57BL/6J) that express Cre-recombinase under the control of the Prrx1 promoter (Prx1-cre), the Pdgfrα promoter (Pdgfrα-cre), and the Dmp1 promoter (Dmp1-cre) were purchased from Jackson Laboratory. $Shn3^{-/-}$[31]and $Shn3^{fl/fl}$[72] mice were previously generated and maintained on a BALB/c and C57BL/6J background, respectively. Wild-type (C57BL/6J) mice, Pdgfrα-GFP, and Rosa26 $^{mT/mG}$ reporter mice, severe combined immunodeficiency (SCID) mice, and TCF/Lef1-HIST1:H2BB/EGFP reporter mice were purchased from The Jackson Laboratory. Mouse genotypes were determined by PCR on tail genomic DNA; primer sequences are available upon request. All animals were used in accordance with the NIH Guide for the Care and Use of Laboratory Animals and were handled according to protocols approved by the University of Massachusetts Chan Medical School Institutional Animal Care and Use Committee (Protocol#: A-202200036).

High-frequency vibration

A portable high-frequency wand was applied to the mandible of both cheeks to produce high-frequency mechanical vibration in alveolar bone, teeth, and periodontal tissues within the mandible. All HFV treatment was applied to cheek skin around the buccal side of the mandible molar for 30 s per day, according to the experiment's purpose and timeline. The portable high-frequency wand delivers a micro-vibration frequency at 200 Hz with 10,000/min vibration. Working voltage and power: 1.5V, 0.1W.

MicroCT and radiography

MicroCT (μCT35; SCANCO Medical AG; Bruttisellen, Switzerland) was used for qualitative and quantitative assessment of bone mass and microarchitecture of alveolar bones and femurs, which was performed by an investigator blinded to the genotypes of the animals under analysis. MicroCT scanning was performed at 55 kVp and 114 mA energy intensity with 300-ms integration time. A specific voxel size of 12 μm was used to measure the mandibular body, molars, and incisors. All images were reconstructed using image matrices of 1024 × 1024 pixels.

For trabecular bone analysis of the distal femur, an upper 2.1-mm region beginning 280 μm proximal to the growth plate was contoured. Additionally, a mid-shaft region of 0.6 mm in length was used to analyze cortical bone. For mandibular bone analysis, the area between the mesial and distal root of the first molar was measured volumetrically through 100 serial images (120 μm span). Specifically, contour lines were drawn between the mesial and distal root of the mandibular first molar to define the alveolar bone region of interest (ROI) in microCT 2D sagittal sections: $Shn3^{-/-}$, $Shn3^{Prx1}$, $Shn3^{Pdgfr\alpha}$, $Shn3^{Dmp1}$, wild-type mice, and AAV-treated OVX mice (100 serial images) or 20-month-old mice (140 serial images).

For the assessment of mineral density and thickness of root dentin or cementum, 40 slices centered on the cut-through of the mesial root in the first molar were measured. The first slice in the sequence was below the pulp chamber when two roots separate to form two distinct channels. The last slice was at the apex of the tooth. For crown dentin and enamel, molar enamel and dentin volume and density were calculated and measured from the cementum-enamel junction to the highest cusp tip. Customized filtering and thresholding were applied to quantify the targeted area within the volume of interest (VOI).

For the assessment of enamel mass, we set the fixed value of 1,000 as a high threshold and increased the low threshold up to 900 to highlight dense segmentation within VOI. For the assessment of dentin mass, we set the fixed value of 900 as a high threshold and increased the low threshold up to 320 to highlight dense segmentation within VOI. 3D reconstruction images were obtained from contoured 2D images by methods based on the distance transformation of the binarized images. Alternatively, the Inveon multimodality 3D visualization program was used to generate fused 3D viewing of multiple static or dynamic volumes of microCT modalities (Siemens Medical Solutions USA, Inc.). All images presented are representative of the respective genotypes ($n > 5$).

The Trident Specimen Radiography system (Hologic, USA) was used to generate detailed radiographic images of the whole mouse body after euthanasia. The X-ray beam intensity was 1 mA 28–30 kV with automatic exposure control for consistent image acquisition.

Histology and histomorphometry

For histological analysis, alveolar bones were dissected from the mice, fixed in 10% neutral buffered formalin for 2 days, and decalcified by 14% tetrasodium EDTA for 2–4 weeks. Tissues were dehydrated by passage through an ethanol series, cleared twice in xylene, embedded in paraffin, and sectioned at a thickness of 6 μm along the coronal plate from anterior to posterior. Decalcified femoral sections were stained with hematoxylin and eosin (H&E), Masson's trichrome, or tartrate-resistant acid phosphatase (TRAP).

For dynamic histomorphometric analysis, 25 mg/kg calcein (Sigma, C0875) and 50 mg/kg alizarin-3-methyliminodiacetic acid (Sigma, A3882) dissolved in 2% sodium bicarbonate solution were subcutaneously injected into mice at 6-day intervals. After fixing in 10% neutral buffered formalin for 2 days, undecalcified mandibular bone samples were embedded in methyl methacrylate, and alveolar bone was sectioned longitudinally (5 μm) and stained with McNeal's trichrome for osteoid assessment and TRAP for osteoclasts.[73] An ROI is defined under the mandibular first molar in the metaphysis and BFR/bone surface (BS), MAR, BS, Ob.S/BS, and osteoclast surface (Oc.S/BS) are measured using the Osteometrics. Measurements were taken on two sections/sample (separated by ∼25 μm) and summed prior to normalization to obtain a single measure/sample in accordance with ASBMR standards.[74] This methodology has undergone extensive quality control and validation, and the results were assessed by two different researchers in a blinded fashion. MAR was calculated by measuring the distance between the calcein-labeled bone (green line) and the alizarin red-labeled bone (red line); this measurement was made at defined sites around the mandibular incisors in five separate mice. The same analyses were performed on the lower incisor for dentin apposition rate.

IHC and immunofluorescence

For IHC analysis, paraffin sections were dewaxed and stained according to the manufacturer's directions, using the Discovery XT automated IHC stainer (Ventana Medical Systems, Inc., Tucson, AZ, USA). CC1 standard buffer (pH 8.4 buffer containing Tris/Borate/EDTA) and inhibitor D (3% H_2O_2, endogenous peroxidase) were used for antigen retrieval and blocking, respectively. Sections were incubated with antibodies specific to SHN3 (PA5-52194, Thermo Fisher, 1:200), SOST (AF1589-SP, R&D systems, 1:100), or DKK1 (21112-1-AP, Proteintech, 1:100) for 40 min at 37 °C, and a secondary antibody for 20 min at 37 °C. Subsequently, they were incubated in SA-HRP D for 16 min at 37 °C and then DAB + H_2O_2 substrate for 8 min, followed by hematoxylin and bluing reagent counterstain at 37 °C. Reaction buffer (pH 7.6 Tris buffer) was used as a washing solution. Stained samples were visualized using an Aperio virtual microscope (Leica Microsystems, USA), and images of the sample were analyzed by the Aperio image scope program (version 12.3.2.8013, Leica Microsystems, USA).

For immunofluorescence analysis, fresh alveolar bone dissected from *Shn3*$^{-/-}$, *Shn3*^{Prx1}, *Shn3*$^{Pdgfr\alpha}$, *Shn3*^{Dmp1}, and wild-type mice and rAAV-treated mice were collected and immediately fixed in ice-cold 4% paraformaldehyde solution for 2 days. Semi-decalcification was carried out for 5 days in 0.5 M EDTA, pH 7.4, at 4 °C with constant shaking (age ≥1 week), and infiltration was followed with a mixture of 20% sucrose phosphate buffer for 1 day and with 25% sucrose phosphate buffer the next day. All samples were embedded in a 50/50 mixture of 25% sucrose solution and OCT compound (Sakura) and cut into 12-μm-thick sagittal sections using a cryostat (Leica). Immunofluorescence staining and analysis were performed as described previously.[73,75] Briefly, after treatment with 0.2% Triton X-100 for 10 min, sections were blocked with 5% donkey serum at room temperature for 30 min and incubated overnight at 4 °C with anti-β-CATENIN antibody (ThermoFisher, PA5-77934, 1:100). Primary antibodies were visualized with donkey anti-rat immunoglobulin (Ig)G Alexa 594 (1:500, Molecular Probes). Nuclei were counterstained with 4',6-diamidino-2-phenylindole (DAPI). An Olympus IX81 confocal microscope or Leica TCS SP5 II Zeiss LSM-880 confocal microscope was used to image samples.

Scanning electron microscopy

Mandibular bones were isolated from 1-month-old *Shn3*^{Pdgfra} and *Shn3*$^{fl/fl}$ mice. They were fixed in 2.5% glutaraldehyde and 1.6% paraformaldehyde in cacodylate buffer (pH 7.2) overnight a 4°C and dehydrated through an ethanol gradient (70%–100%) and 100% acetone, followed by embedding in Spur's epoxy resin and polymerized at 68°C of 48 h. The embedded mandibles were sectioned at the first molar using a slow-speed diamond saw and finally polished using Pol Metal Polish DKK100 (Pol, Denmark). The polished surfaces were coated with 8 nm of Gold-Palladium and imaged using a ThermoFisher, Quanta 200 FESEM (Hillsborough, OR) 10 Kv accelerating voltage.

AAV treatment in a mouse model of postmenopausal osteoporosis

Mouse models of postmenopausal osteoporosis were generated by anesthetizing and bilaterally ovariectomizing (OVX) 3-month-old female mice (Jackson Laboratory, C57BL/6J). Four weeks after the surgery, sham or OVX mice were i.v. (2.5×10^{13} vector genomes [vg]/kg) or PL (2.5×10^{12} vg/kg) injected with rAAV9 or dss.rAAV9 carrying *egfp*, *amiR-ctrl*, *amiR-SHN3,* or *amiR-SOST/hs-amiR-SHN3*. Seven weeks after the injection, mice were subcutaneously injected with calcein and alizarin-3-methyliminodiacetic acid at 6-day intervals for dynamic histomorphometric analysis. Non-labeled mice were used to monitor EGFP expression using the IVIS-100 optical imaging on frozen sections.

AAV treatment of human skeletal organoid in xenograft mice

Human BMSCs were seeded on hydroxyapatite (HA)-scaffold (Osteogene Tech), cultured under osteogenic conditions for 2 days,

and implanted into the interscapular fat pads of 3-month-old immunodeficient SCID mice. One week later, rAAV9 (2.5×10^{12} vg/kg) carrying *hs-amiR-ctrl* or *hs-amiR-hSHN3* was injected into the implantation site (Figure 3D). Four weeks later, the implanted HA-scaffold was visualized by radiography and then, EGFP expression in the scaffold was assessed by the IVIS optical imaging system. Bone and collagen formation was assessed by microCT, histology, and SEM analyses.

DATA AND CODE AVAILABILITY

The data that support the findings of this study are available in the supporting information of this article.

SUPPLEMENTAL INFORMATION

Supplemental information can be found online at https://doi.org/10.1016/j.ymthe.2024.06.036.

ACKNOWLEDGMENTS

We thank Dr. Steven Neier for thoughtful discussion, Drs. Laurie Glimcher and Melanie Trombly for reviewing the manuscript, Ms. Agustina Rodriguez and Ms. Emma Mayer for technical support, and many individuals who provided valuable reagents. Additionally, we thank Dr. Daniel Oh for providing hydroxyapatite (HA)-based scaffold (Osteogene Tech, Inc). We also thank the Electron Microscopy and the Flow Cytometry Core Facilities funded in part by NIH core instrument grants. G.G. holds support from grants under the NIH (R01NS076991, P01HL131471, R01AI121135, UG3HL 147367, R01HL097088, R01HL152723, U19AI149646, and UH3H L147367). J.-H.S. holds support from NIAMS of the NIH (R01AR068983, R21AR073331).

AUTHOR CONTRIBUTIONS

C.L. designed, executed, and interpreted the experiments. J.X. and H.M. designed and generated all of the AAVs used in this work. Y.-S.Y. and Z.C. performed the skeletal assessments. A.A.J. and D.C. performed mouse experiments. G.G. and J.-H.S. supervised the research and prepared the manuscript.

DECLARATION OF INTERESTS

G.G. and J.H.S. have submitted a patent application concerning the methodology described in this study. G.G. and J.H.S. are scientific co-founders of AAVAA Therapeutics and hold equity in this company. G.G. is also a scientific co-founder of Voyager Therapeutics, Adrenas Therapeutics, and Aspa Therapeutics, and holds equity in these companies. G.G. is an inventor on patents with potential royalties licensed to Voyager Therapeutics, Adrenas Therapeutics, Aspa Therapeutics, and other biopharmaceutical companies.

REFERENCES

1. HASSELL, T.M. (1993). Tissues and cells of the periodontium. Periodontology, 9–38.
2. Avery, J.K., and Chiego, D.J. (2007). Essentials of Oral Histology and Embryology: A Clinical Approach (Reed Elsevier).
3. CHO, M.I., and Garant, P.R. (2000). Development and general structure of the periodontium. Periodontology, 9–27.
4. Omi, M., and Mishina, Y. (2020). Role of osteoclasts in oral homeostasis and jawbone diseases. Oral Sci. Int. *18*, 14–27.
5. Devlin, H., and Ferguson, M. (1991). Alveolar ridge resorption and mandibular atrophy. A review of the role of local and systemic factors. Br. Dent. J. *170*, 101–104.
6. Jeffcoat, M.K., and Chesnut 3rd, C. (1993). Systemic osteoporosis and oral bone loss: evidence shows increased risk factors. J. Am. Dent. Assoc. *124*, 49–56.
7. von Wowern, N. (2001). General and oral aspects of osteoporosis: a review. Clin. Oral Investig. *5*, 71–82.
8. Jaffin, R.A., and Berman, C.L. (1991). The excessive loss of Branemark fixtures in type IV bone: a 5-year analysis. J. Periodontol. *62*, 2–4.
9. van Steenberghe, D., Lekholm, U., Bolender, C., Folmer, T., Henry, P., Herrmann, I., Higuchi, K., Laney, W., Lindén, U., and Åstrand, P. (1990). The Applicability of Osseointegrated Oral Implants in the Rehabilitation of Partial Edentulism: A Prospective Multicenter Study on 558 Fixtures. Int. J. Oral Maxillofacial Implants *5*, 272–281.
10. Yamaza, T., Miura, Y., Bi, Y., Liu, Y., Akiyama, K., Sonoyama, W., Patel, V., Gutkind, S., Young, M., Gronthos, S., et al. (2008). Pharmacologic stem cell based intervention as a new approach to osteoporosis treatment in rodents. PloS one *3*, e2615.
11. Kao, S.T., and Scott, D.D. (2007). A review of bone substitutes. Oral Maxillofac. Surg. Clin. North Am. *19*, 513–521.
12. Kumar, P., Vinitha, B., and Fathima, G. (2013). Bone grafts in dentistry. J. Pharm. Bioallied Sci. *5*, S125–S127.
13. Lundgren, D., Sennerby, L., Falk, H., Friberg, B., and Nyman, S. (1994). The use of a new bioresorbable barrier for guided bone regeneration in connection with implant installation. Case reports. Clin. Oral Implants Res. *5*, 177–184.
14. Sheikh, Z., Hamdan, N., Ikeda, Y., Grynpas, M., Ganss, B., and Glogauer, M. (2017). Natural graft tissues and synthetic biomaterials for periodontal and alveolar bone reconstructive applications: a review. Biomater. Res. *21*, 9–20.
15. Iwamoto, J., Sato, Y., Takeda, T., and Matsumoto, H. (2008). Hip fracture protection by alendronate treatment in postmenopausal women with osteoporosis: a review of the literature. Clin. Interv. Aging *3*, 483–489.
16. Cummings, S.R., Martin, J.S., McClung, M.R., Siris, E.S., Eastell, R., Reid, I.R., Delmas, P., Zoog, H.B., Austin, M., Wang, A., et al. (2009). Denosumab for prevention of fractures in postmenopausal women with osteoporosis. N. Engl. J. Med. *361*, 756–765.
17. Esbrit, P., and Alcaraz, M.J. (2013). Current perspectives on parathyroid hormone (PTH) and PTH-related protein (PTHrP) as bone anabolic therapies. Biochem. Pharmacol. *85*, 1417–1423.
18. Weaver, C., Alexander, D., Boushey, C., Dawson-Hughes, B., Lappe, J.M., LeBoff, M., Liu, S., Looker, A., Wallace, T., and Wang, D. (2016). Calcium plus vitamin D supplementation and risk of fractures: an updated meta-analysis from the National Osteoporosis Foundation. Osteoporos. Int. *27*, 367–376.
19. Borumandi, F., Aghaloo, T., Cascarini, L., Gaggl, A., and Fasanmade, K. (2015). Anti-resorptive drugs and their impact on maxillofacial bone among cancer patients. Anticancer. Agents Med. Chem. *15*, 736–743.
20. Landesberg, R., Woo, V., Cremers, S., Cozin, M., Marolt, D., Vunjak-Novakovic, G., Kousteni, S., and Raghavan, S. (2011). Potential pathophysiological mechanisms in osteonecrosis of the jaw. Ann. N. Y. Acad. Sci. *1218*, 62–79.
21. Baron, R., Ferrari, S., and Russell, R.G.G. (2011). Denosumab and bisphosphonates: different mechanisms of action and effects. Bone *48*, 677–692.
22. Becker, W., Hujoel, P.P., Becker, B.E., and Willingham, H. (2000). Osteoporosis and implant failure: an exploratory case-control study. J. Periodontol. *71*, 625–631.
23. Rodella, L.F., Favero, G., and Labanca, M. (2011). Biomaterials in maxillofacial surgery: membranes and grafts. Int. J. Biomed. Sci. *7*, 81–88.
24. Bulcha, J.T., Wang, Y., Ma, H., Tai, P.W.L., and Gao, G. (2021). Viral vector platforms within the gene therapy landscape. Signal Transduct. Target. Ther. *6*, 53. https://doi.org/10.1038/s41392-021-00487-6.
25. Wang, D., Tai, P.W.L., and Gao, G. (2019). Adeno-associated virus vector as a platform for gene therapy delivery. Nat. Rev. Drug Discov. *18*, 358–378. https://doi.org/10.1038/s41573-019-0012-9.
26. Yang, Y.S., Xie, J., Wang, D., Kim, J.M., Tai, P.W.L., Gravallese, E., Gao, G., and Shim, J.H. (2019). Bone-targeting AAV-mediated silencing of Schnurri-3 prevents bone loss

in osteoporosis. Nat. Commun. *10*, 2958. https://doi.org/10.1038/s41467-019-10809-6.

27. Shim, J.-H., Greenblatt, M.B., Zou, W., Huang, Z., Wein, M.N., Brady, N., Hu, D., Charron, J., Brodkin, H.R., Petsko, G.A., et al. (2013). Schnurri-3 regulates ERK downstream of WNT signaling in osteoblasts. J. Clin. Invest. *123*, 4010–4022.

28. Xu, R., Yallowitz, A., Qin, A., Wu, Z., Shin, D.Y., Kim, J.M., Debnath, S., Ji, G., Bostrom, M.P., Yang, X., et al. (2018). Targeting skeletal endothelium to ameliorate bone loss. Nat. Med. *24*, 823–833. https://doi.org/10.1038/s41591-018-0020-z.

29. Semënov, M., Tamai, K., and He, X. (2005). SOST is a ligand for LRP5/LRP6 and a Wnt signaling inhibitor. J. Biol. Chem. *280*, 26770–26775.

30. Winkler, D.G., Sutherland, M.K., Geoghegan, J.C., Yu, C., Hayes, T., Skonier, J.E., Shpektor, D., Jonas, M., Kovacevich, B.R., Staehling-Hampton, K., et al. (2003). Osteocyte control of bone formation via sclerostin, a novel BMP antagonist. EMBO J. *22*, 6267–6276.

31. Jones, D.C., Wein, M.N., Oukka, M., Hofstaetter, J.G., Glimcher, M.J., and Glimcher, L.H. (2006). Regulation of adult bone mass by the zinc finger adapter protein Schnurri-3. Science *312*, 1223–1227.

32. Yao, Y., Kauffmann, F., Maekawa, S., Sarment, L.V., Sugai, J.V., Schmiedeler, C.A., Doherty, E.J., Holdsworth, G., Kostenuik, P.J., and Giannobile, W.V. (2020). Sclerostin antibody stimulates periodontal regeneration in large alveolar bone defects. Sci. Rep. *10*, 16217.

33. Glantschnig, H., Scott, K., Hampton, R., Wei, N., McCracken, P., Nantermet, P., Zhao, J.Z., Vitelli, S., Huang, L., Haytko, P., et al. (2011). A rate-limiting role for Dickkopf-1 in bone formation and the remediation of bone loss in mouse and primate models of postmenopausal osteoporosis by an experimental therapeutic antibody. J. Pharmacol. Exp. Ther. *338*, 568–578.

34. Grisanti, M., Niu, Q., Fan, W., Asuncion, F., Lee, J., Steavenson, S., Chen, Q., Li, J., Geng, Z., and Kostenuik, P. (2006). Dkk-1 inhibition increases bone mineral density in rodents. J. bone mineral Res. *21*. amer soc bone & mineral res 2025 m st, nw, ste 800, WASHINGTON, DC 20036 ….

35. Brun, J., Andreasen, C.M., Ejersted, C., Andersen, T.L., Caverzasio, J., and Thouverey, C. (2020). PDGF receptor signaling in osteoblast lineage cells controls bone resorption through upregulation of Csf1 expression. J. Bone Miner. Res. *35*, 2458–2469.

36. Morikawa, S., Mabuchi, Y., Kubota, Y., Nagai, Y., Niibe, K., Hiratsu, E., Suzuki, S., Miyauchi-Hara, C., Nagoshi, N., Sunabori, T., et al. (2009). Prospective identification, isolation, and systemic transplantation of multipotent mesenchymal stem cells in murine bone marrow. J. Exp. Med. *206*, 2483–2496.

37. Muzumdar, M.D., Tasic, B., Miyamichi, K., Li, L., and Luo, L. (2007). A global double-fluorescent Cre reporter mouse. genesis *45*, 593–605.

38. Xie, J., Tai, P.W., Brown, A., Gong, S., Zhu, S., Wang, Y., Li, C., Colpan, C., Su, Q., He, R., et al. (2020). Effective and accurate gene silencing by a recombinant AAV-compatible microRNA scaffold. Mol. Ther. *28*, 422–430.

39. Xie, J., Mao, Q., Tai, P.W., He, R., Ai, J., Su, Q., Zhu, Y., Ma, H., Li, J., Gong, S., et al. (2017). Short DNA hairpins compromise recombinant adeno-associated virus genome homogeneity. Mol. Ther. *25*, 1363–1374.

40. Yang, Y.-S., Xie, J., Wang, D., Kim, J.-M., Tai, P.W., Gravallese, E., Gao, G., and Shim, J.-H. (2019). Bone-targeting AAV-mediated silencing of Schnurri-3 prevents bone loss in osteoporosis. Nat. Commun. *10*, 2958.

41. Yang, Y.S., Xie, J., Chaugule, S., Wang, D., Kim, J.M., Kim, J., Tai, P.W.L., Seo, S.K., Gravallese, E., Gao, G., and Shim, J.H. (2020). Bone-Targeting AAV-Mediated Gene Silencing in Osteoclasts for Osteoporosis Therapy. Mol. Ther. Methods Clin. Dev. *17*, 922–935. https://doi.org/10.1016/j.omtm.2020.04.010.

42. Martínez-Maestre, M.Á., González-Cejudo, C., Machuca, G., Torrejón, R., and Castelo-Branco, C. (2010). Periodontitis and osteoporosis: a systematic review. Climacteric. *13*, 523–529.

43. Buencamino, M., Palomo, L., and Thacker, H.L. (2009). How menopause affects oral health, and what we can do about it. Cleve. Clin. J. Med. *76*, 467–475.

44. Bouxsein, M.L., Myers, K.S., Shultz, K.L., Donahue, L.R., Rosen, C.J., and Beamer, W.G. (2005). Ovariectomy-induced bone loss varies among inbred strains of mice. J. Bone Miner. Res. *20*, 1085–1092. https://doi.org/10.1359/JBMR.050307.

45. Mullard, A. (2016). Merck &Co. drops osteoporosis drug odanacatib. Nat. Rev. Drug Discov. *15*, 669. https://doi.org/10.1038/nrd.2016.207.

46. Saag, K.G., Petersen, J., Brandi, M.L., Karaplis, A.C., Lorentzon, M., Thomas, T., Maddox, J., Fan, M., Meisner, P.D., and Grauer, A. (2017). Romosozumab or Alendronate for Fracture Prevention in Women with Osteoporosis. N. Engl. J. Med. *377*, 1417–1427. https://doi.org/10.1056/NEJMoa1708322.

47. Lagos-Quintana, M., Rauhut, R., Yalcin, A., Meyer, J., Lendeckel, W., and Tuschl, T. (2002). Identification of tissue-specific microRNAs from mouse. Curr. Biol. *12*, 735–739.

48. Chang, J., Nicolas, E., Marks, D., Sander, C., Lerro, A., Buendia, M.A., Xu, C., Mason, W.S., Moloshok, T., Bort, R., et al. (2004). miR-122, a mammalian liver-specific microRNA, is processed from hcr mRNA and maydownregulate the high affinity cationic amino acid transporter CAT-1. RNA Biol. *1*, 106–113.

49. Van Rooij, E., Sutherland, L.B., Liu, N., Williams, A.H., McAnally, J., Gerard, R.D., Richardson, J.A., and Olson, E.N. (2006). A signature pattern of stress-responsive microRNAs that can evoke cardiac hypertrophy and heart failure. Proc. Natl. Acad. Sci. USA *103*, 18255–18260.

50. Bonewald, L.F., and Johnson, M.L. (2008). Osteocytes, mechanosensing and Wnt signaling. Bone *42*, 606–615.

51. Ferrer-Vaquer, A., Piliszek, A., Tian, G., Aho, R.J., Dufort, D., and Hadjantonakis, A.K. (2010). A sensitive and bright single-cell resolution live imaging reporter of Wnt/ß-catenin signaling in the mouse. BMC Dev. Biol. *10*, 121. https://doi.org/10.1186/1471-213X-10-121.

52. Cadigan, K.M., and Waterman, M.L. (2012). TCF/LEFs and Wnt signaling in the nucleus. Cold Spring Harb. Perspect. Biol. *4*, a007906.

53. Alikhani, M., Khoo, E., Alyami, B., Raptis, M., Salgueiro, J., Oliveira, S., Boskey, A., and Teixeira, C. (2012). Osteogenic effect of high-frequency acceleration on alveolar bone. J. Dent. Res. *91*, 413–419.

54. Benjakul, S., Leethanakul, C., and Jitpukdeebodintra, S. (2019). Low magnitude high frequency vibration induces RANKL via cyclooxygenase pathway in human periodontal ligament cells in vitro. J. Oral Biol. Craniofac. Res. *9*, 251–255.

55. Benjakul, S., Jitpukdeebodintra, S., and Leethanakul, C. (2018). Effects of low magnitude high frequency mechanical vibration combined with compressive force on human periodontal ligament cells in vitro. Eur. J. Orthod. *40*, 356–363.

56. Alikhani, M., Alikhani, M., Alansari, S., Almansour, A., Hamidaddin, M.A., Khoo, E., Lopez, J.A., Nervina, J.M., Nho, J.Y., Oliveira, S.M., et al. (2019). Therapeutic effect of localized vibration on alveolar bone of osteoporotic rats. PLoS One *14*, e0211004.

57. Oh, W.-T., Yang, Y.-S., Xie, J., Ma, H., Kim, J.-M., Park, K.-H., Oh, D.S., Park-Min, K.-H., Greenblatt, M.B., Gao, G., and Shim, J.H. (2023). WNT-modulating gene silencers as a gene therapy for osteoporosis, bone fracture, and critical-sized bone defects. Mol. Ther. *31*, 435–453.

58. Glass, D.A., , 2nd, Bialek, P., Ahn, J.D., Starbuck, M., Patel, M.S., Clevers, H., Taketo, M.M., Long, F., McMahon, A.P., Lang, R.A., and Karsenty, G. (2005). Canonical Wnt signaling in differentiated osteoblasts controls osteoclast differentiation. Dev. Cell *8*, 751–764.

59. Elsalanty, M.E., and Genecov, D.G. (2009). Bone grafts in craniofacial surgery. Craniomaxillofac. Trauma Reconstr. *2*, 125–134.

60. Sodek, J., and Mckee, M.D. (2000). Molecular and cellular biology of alveolar bone. Periodontology *24*, 99–126.

61. Sassouni, V. (1969). A classification of skeletal facial types. Am. J. Orthod. *55*, 109–123.

62. Herring, S.W. (2007). Masticatory muscles and the skull: a comparative perspective. Arch. Oral Biol. *52*, 296–299.

63. Lin, C., Greenblatt, M.B., Gao, G., and Shim, J.-H. (2024). Development of AAV-Mediated Gene Therapy Approaches to Treat Skeletal Diseases. Hum. Gene Ther. *35*, 317–328.

64. Shim, J.H., Greenblatt, M.B., Zou, W., Huang, Z., Wein, M.N., Brady, N., Hu, D., Charron, J., Brodkin, H.R., Petsko, G.A., et al. (2013). Schnurri-3 regulates ERK downstream of WNT signaling in osteoblasts. J. Clin. Invest. *123*, 4010–4022. https://doi.org/10.1172/JCI69443.

65. Grimm, D., Streetz, K.L., Jopling, C.L., Storm, T.A., Pandey, K., Davis, C.R., Marion, P., Salazar, F., and Kay, M.A. (2006). Fatality in mice due to oversaturation of cellular microRNA/short hairpin RNA pathways. Nature *441*, 537–541. https://doi.org/10.1038/nature04791.

66. McBride, J.L., Boudreau, R.L., Harper, S.Q., Staber, P.D., Monteys, A.M., Martins, I., Gilmore, B.L., Burstein, H., Peluso, R.W., Polisky, B., et al. (2008). Artificial miRNAs mitigate shRNA-mediated toxicity in the brain: implications for the therapeutic development of RNAi. Proc. Natl. Acad. Sci. USA *105*, 5868–5873. https://doi.org/10.1073/pnas.0801775105.

67. Xie, J., Tai, P.W.L., Brown, A., Li, C., Zamore, P.D., and Gao, G. (2018). A Novel rAAV-amiRNA Platform Enables Potent in Vivo Gene Silencing and a Ten-fold Enhancement of On-Target Specificity over Conventional shRNA Vectors (American Society of Gene and Cell Therapy 21st Annual Meeting).

68. Alikhani, M., Alansari, S., Hamidaddin, M.A., Sangsuwon, C., Alyami, B., Thirumoorthy, S.N., Oliveira, S.M., Nervina, J.M., and Teixeira, C.C. (2018). Vibration paradox in orthodontics: Anabolic and catabolic effects. PLoS One *13*, e0196540.

69. Yamaza, T., Ren, G., Akiyama, K., Chen, C., Shi, Y., and Shi, S. (2011). Mouse mandible contains distinctive mesenchymal stem cells. J. Dent. Res. *90*, 317–324.

70. Yang, Y.-S., Xie, J., Chaugule, S., Wang, D., Kim, J.-M., Kim, J., Tai, P.W., Seo, S.-k., Gravallese, E., Gao, G., and Shim, J.H. (2020). Bone-targeting AAV-mediated gene silencing in osteoclasts for osteoporosis therapy. Mol. Ther. Methods Clin. Dev. *17*, 922–935.

71. Xie, J., Mao, Q., Tai, P.W.L., He, R., Ai, J., Su, Q., Zhu, Y., Ma, H., Li, J., Gong, S., et al. (2017). Short DNA Hairpins Compromise Recombinant Adeno-Associated Virus Genome Homogeneity. Mol. Ther. *25*, 1363–1374. https://doi.org/10.1016/j.ymthe.2017.03.028.

72. Jones, D.C., Schweitzer, M.N., Wein, M., Sigrist, K., Takagi, T., Ishii, S., and Glimcher, L.H. (2010). Uncoupling of growth plate maturation and bone formation in mice lacking both Schnurri-2 and Schnurri-3. Proc. Natl. Acad. Sci. USA *107*, 8254–8258.

73. Fukuda, T., Takeda, S., Xu, R., Ochi, H., Sunamura, S., Sato, T., Shibata, S., Yoshida, Y., Gu, Z., Kimura, A., et al. (2013). Sema3A regulates bone-mass accrual through sensory innervations. Nature *497*, 490–493.

74. Parfitt, A.M., Drezner, M.K., Glorieux, F.H., Kanis, J.A., Malluche, H., Meunier, P.J., Ott, S.M., and Recker, R.R. (1987). Bone histomorphometry: standardization of nomenclature, symbols, and units: report of the ASBMR Histomorphometry Nomenclature Committee. J. Bone Miner. Res. *2*, 595–610.

75. Xu, R., Zhang, C., Shin, D.Y., Kim, J.M., Lalani, S., Li, N., Yang, Y.S., Liu, Y., Eiseman, M., Davis, R.J., et al. (2017). c-Jun N-Terminal Kinases (JNKs) are critical mediators of osteoblast activity in vivo. J. Bone Miner. Res. *32*, 1811–1815.